PHYSICAL REVIEW C, VOLUME 61, 024901

Relativistic nuclear collisions at 10A GeV energies from p+Be to Au+Au with the hadronic cascade model

Y. Nara,[1,2] N. Otuka,[3] A. Ohnishi,[3] K. Niita,[4] and S. Chiba[1]
[1]*Advanced Science Research Center, Japan Atomic Energy Research Institute, Tokai, Naka, Ibaraki 319-1195, Japan*
[2]*Physics Department, Brookhaven National Laboratory, Upton, New York 11973*
[3]*Division of Physics, Graduate School of Science, Hokkaido University, Sapporo 060-0810, Japan*
[4]*Research Organization for Information Science and Technology, Tokai, Naka, Ibaraki 319-1195, Japan*

(Received 23 April 1999; published 22 December 1999)

A hadronic cascade model based on resonances and strings is used to study mass dependence of relativistic nuclear collisions from p+Be to Au+Au at AGS energies ($\sim$10A GeV) systematically. Hadron transverse momentum and rapidity distributions obtained with both cascade calculations and Glauber-type calculations are compared with experimental data, leading to a detailed discussion concerning the importance of rescattering among hadrons. We find good agreement with the experimental data without any change of model parameters with the cascade model. It is found that rescattering is of importance both for the explanation of the high transverse momentum tail and for the multiplicity of produced particles.

PACS number(s): 25.75.Gz, 14.20.Gk, 24.85.+p

I. INTRODUCTION

There is now much interest in studying strongly interacting matter at high density and/or temperature created in high energy nuclear collisions. Indeed, at high densities and/or temperatures, QCD predicts the chiral symmetry restoration and quark deconfinement. How can we create such matter? At present, high energy heavy ion collision is considered to be a unique way to create such dense and hot matter in the laboratory. In order to find such a new form of nuclear matter, several heavy ion experiments have been and are being performed with Si(14.6A GeV/c) or Au(11.6A GeV/c) beam at BNL Alternating Gradient Synchrotron (AGS) and with the O(200A GeV/c), S(200A GeV/c) or Pb(158A GeV/c) beam at CERN Super Proton Synchrotron (SPS).

Since high energy heavy ion collisions lead to a huge number of final states, many event generators have been proposed to explore these high energy nuclear collisions, with the aid of the Monte-Carlo realization of complex processes. In these event generators, there are mainly three categories of models. The models in the first category assume Glauber geometry for the treatment of AA collisions. For example, FRITIOF [1], LUCIAE [2], VENUS [3], HIJING [4], DPM [5], HIJET [6], and LEXUS [7] belong to this category. Final interaction among hadrons are included in VENUS, HIJET, and LUCIAE. In these models, main quantum features during the multiple scattering are preserved within the eikonal approximation, and efficiently fast calculations are possible. However, these approaches are mainly designed for extremely high energy collisions ($\sqrt{s}>10A$ GeV).

The models in the second category (parton cascade models), such as VNI [8] and ZPC [9], have been recently developed to implement the interaction among partons to study the space-time evolution of partons produced in high energy nuclear collisions. These models were originally designed to describe ultrarelativistic heavy ion collisions at collider energies, such as BNL Relativistic Heavy Ion Collider (RHIC) and CERN Large Hadron Collider (LHC), and have met with some success in describing heavy ion collisions at CERN SPS energies [10].

The third category of model is a transport model which is often referred to as ''hadronic cascade.'' For example, RQMD [11,12], QGSM [13], ARC [14], ART [15], UrQMD [16], and HSD [17] can be categorized here. They have been successfully used to describe many aspects of high energy heavy ion collisions in a wide range of incident energies. For the description of AA collisions in hadronic cascade models, the trajectories of all hadrons as well as resonances including produced particles are followed explicitly as a function of time. Nuclear collisions are modeled by the sum of independent hadron-hadron (hh) collisions without interferences. Two particles are made to collide if their closest distance is smaller than $\sqrt{\sigma(s)/\pi}$, where $\sigma(s)$ represents the total cross section at the c.m. energy $\sqrt{s}$. As a result of the hh collision, secondary particles will be produced according to the specific model with some formation time. One of the most distinct differences among these models may be the method of implementing hadronic degrees of freedom. In RQMD and UrQMD, many established hadronic resonances are explicitly propagated in space-time, while ARC, ART, and HSD do not include higher hadronic resonances. Although both modelings seem to give similar results if we see the final hadronic spectra inclusively, we expect thermodynamic quantities like pressure or temperature before freeze-out predicted by those models would be different from each other [18]. Another difference is the treatment of multiparticle production. The string model is adapted in RQMD, QGSM, UrQMD, and HSD, while in ARC and ART, final states are sampled according to the direct parameterization of the experimental data. The hadronic cascade model based on the string phenomenology implies that some partonic degrees of freedom play some roles in reaction dynamics implicitly. In fact, the estimation of partonic degrees of freedom has been done recently within UrQMD [19]. ARC [14] has shown that a ''pure'' hadronic model can describe the data at AGS energies. At collider energies, however, explicit treatments of partonic degrees of freedom will be necessary.

The main purpose of this work is to perform systematic analyses of collisions from pA to massive AA systems at AGS energies, for which high-quality systematic experimental data are available [41,42], within the hadronic cascade model JAM1.0, which has been developed recently based on resonances, strings, and pQCD.

The main features included in JAM are as follows. (1) At low energies, inelastic hh collisions are modeled by the resonance productions based on the idea from RQMD and UrQMD. (2) Above the resonance region, soft string excitation is implemented along the lines of the HIJING model [4]. (3) Multiple minijet production is also included in the same way as the HIJING model in which jet cross section and the number of jets are calculated using an eikonal formalism for perturbative QCD (pQCD) and hard parton-parton scatterings with initial and final state radiation are simulated using the PYTHIA [20] program. (4) Rescattering of hadrons which have original constituent quarks can occur with other hadrons assuming the additive quark cross section within a formation time. Since these features of the present hadronic cascade model JAM1.0, enable us to explore heavy ion collisions in a wide energy range, from 100A MeV to RHIC energies, in a unified way, it is a big challenge for us to make systematic analyses in these energies. In this paper, we focus on the mass dependence of the collision system at AGS energies. Other applications at higher energies are found elsewhere [21].

The outline of this paper is as follows. We will present a detailed description of cross sections and modeling of inelastic processes for hh collisions in Sec. II, because elementary hh processes are essential inputs for the hadronic cascade model. In Sec. III, we first study the transverse momentum distributions of protons, pions, and kaons in $p+$Be, $p+$Al, $p+$Cu, $p+$Au, Si$+$A, Si$+$Cu, and Si$+$Au collisions at the laboratory incident momentum of 14.6A GeV/c. We discuss the role of rescattering by comparing the cascade model results with the Glauber-type calculations. We then discuss the collision dynamics for truly heavy ion colliding system Au$+$Au collisions. The summary and outlook are given in Sec. IV.

II. MODEL DESCRIPTION

In this section, we present the assumptions and parameters of our model together with the inclusive and the exclusive hh data including incident energy dependence.

A. Main components of the model

The main components of our model are as follows. (1) The nuclear collision is assumed to be described by the sum of independent binary hh collisions. Each hh collision is realized by the closest distance approach. In this work, no mean field is included, therefore the trajectory of each hadron is straight in between two-body collisions, decays, or absorptions. (2) The initial position of each nucleon is sampled by the parametrized distribution of nuclear density.

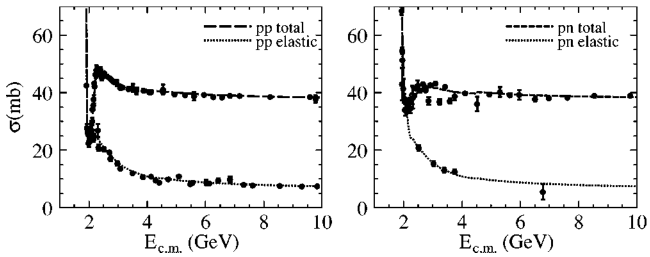

FIG. 1. The fitted total and elastic pp and pn cross sections which are used in the code together with measured data taken from the Particle Data Group [28]. The CERN HERA and COMPAS group parameterizations are used at high energy [28].

Fermi motion of nucleons is assigned according to the local Fermi momentum. (3) All established hadronic states, including resonances, are explicitly included with explicit isospin states as well as their antiparticles. All of them can propagate in space-time. (4) The inelastic hh collisions produce resonances at low energies while at high energies ($\gtrsim 4$ GeV in BB collisions $\gtrsim 3$ GeV in MB collisions, and $\gtrsim 2$ GeV in MM collisions) color strings are formed that decay into hadrons according to the Lund string model [20]. Formation time is assigned to hadrons from string fragmentation. Formation point and time are determined by assuming a yo-yo formation point. This choice gives the formation time of roughly 1 fm/c with string tension $\kappa = 1$ GeV/fm. (5) Hadrons which have original constituent quarks can scatter with other hadrons assuming the additive quark cross section within a formation time. The importance of this quark(diquark)-hadron interaction for the description of baryon stopping at CERN SPS energies was reported by Frankfurt group [11,16]. (6) Pauli blocking for the final nucleons in two-body collisions is also considered. (7) We do not include any medium effects such as string fusion to rope [3,11], medium modified cross sections, and in-medium mass shift. All results which will be presented in this paper are those obtained from the free cross sections and free masses as inputs.

B. Baryon-baryon interactions

Let us start with a detailed explanation of the resonance model for baryon-baryon (BB) collisions implemented in our model. We assume that inelastic BB collisions are described by the resonance formations and their decays below c.m. energy $\sqrt{s} < 4$ GeV and at higher colliding energies, string formation and their fragmentation into hadrons are included based on a similar picture to that in the RQMD [12] and the UrQMD models [16]. The total and elastic pp and pn cross sections are well known. Fitted cross sections and experimental data are shown in Fig. 1. Inelastic cross sections are assumed to be filled up with the resonance formations up to $\sqrt{s} = 3-4$ GeV. At higher energies, the difference between the experimental inelastic cross section and resonance formation cross sections is assigned to the string formation.

The following nonstrange baryonic resonance excitation channels are implemented for the nucleon-nucleon scattering in our model: (1) $NN \to N\Delta(1232)$, (2) $NN \to NN^*$, (3)

TABLE I. Resonance cross section parameters for $I=1$. π_s denotes *s*-wave pion production.

Channel	a	b	c	d	$\sqrt{s_{th}}$
$\sigma_1(NN\rightarrow NN^*)$	24.94700	2.48150	2.63330	0.425358	2.162
$\sigma_1(NN\rightarrow\Delta(1232)\Delta(1232))$	7.63181	1.41140	2.67784	0.311722	2.252
$\sigma_1(NN\rightarrow N\Delta^*)$	8.01615	2.74161	3.34503	0.259703	2.340
$\sigma_1(NN\rightarrow N^*\Delta(1232))$	13.14580	2.06775	2.75682	0.247810	2.300
$\sigma_1(NN\rightarrow\Delta(1232)\Delta^*)$	19.63220	2.01946	2.80619	0.297073	2.528
$\sigma_1(NN\rightarrow N^*N^*)$	11.67320	2.31682	2.96359	0.259223	2.438
$\sigma_1(NN\rightarrow N^*\Delta^*)$	2.99086	2.29380	3.54392	0.090438	2.666
$\sigma_1(NN\rightarrow\Delta^*\Delta^*)$	35.13780	2.25498	3.14299	0.215611	2.804
$\sigma_1(NN\rightarrow NN\pi_s)$	15.644100	1.675220	2.07706	0.658047	2.014

$NN\rightarrow\Delta(1232)\Delta(1232)$, (4) $NN\rightarrow N\Delta^*$, (5) $NN\rightarrow N^*\Delta(1232)$, (6) $NN\rightarrow\Delta(1232)\Delta^*$, (7) $NN\rightarrow N^*N^*$, (8) $NN\rightarrow N^*\Delta^*$, (9) $NN\rightarrow\Delta^*\Delta^*$.

Here N^* and Δ^* represent higher baryonic states below 2 GeV/c^2. The pp and pn cross sections are calculated from each isospin component $\sigma(I)$ (in some cases we ignore the interferences between different amplitudes):

$$\sigma(h_1h_2\rightarrow h_3h_4)=\sum_I |C(h_1h_2,I)|^2|C(h_3h_4,I)|^2\sigma(I), \tag{1}$$

where $C(h_ih_j,I)$ is isospin Clebsch-Gordon coefficients. For N^* and Δ^* production, the sum of production cross sections of several resonance species [$N(1440)\sim N(1990)$ for N^* and $\Delta(1600)\sim\Delta(1950)$ for Δ^*] are parametrized, and resonance species are chosen afterward (see below). The strength of each branch $\sigma(I)$ is determined from the exclusive pion production data [22]. Isospin $I=1$ component for NN collisions can be extracted from the pp reactions. We assume that isospin $I=0$ components are determined from the pn reactions: then the explicit forms of cross sections in different isospin channels can be written as follows:

$$\sigma(pp\rightarrow p\Delta^+)=\frac{1}{4}\sigma(I=1),\quad \sigma(pn\rightarrow n\Delta^+)=\frac{1}{4}\sigma(I=1), \tag{2}$$

$$\sigma(pp\rightarrow n\Delta^{++})=\frac{3}{4}\sigma(I=1),\quad \sigma(pn\rightarrow p\Delta^0)=\frac{1}{4}\sigma(I=1), \tag{3}$$

$$\sigma(pp\rightarrow pp^*)=\sigma(I=1),$$

$$\sigma(pn\rightarrow np^*)=\frac{1}{4}\sigma(I=1)+\frac{1}{4}\sigma(I=0), \tag{4}$$

$$\sigma(pp\rightarrow\Delta^+\Delta^+)=\frac{2}{5}\sigma(I=1),$$

$$\sigma(pn\rightarrow\Delta^0\Delta^+)=\frac{1}{20}\sigma(I=1)+\frac{1}{4}\sigma(I=0), \tag{5}$$

$$\sigma(pp\rightarrow\Delta^0\Delta^{++})=\frac{3}{5}\sigma(I=1),$$

$$\sigma(pn\rightarrow\Delta^-\Delta^{++})=\frac{9}{20}\sigma(I=1)+\frac{1}{4}\sigma(I=0). \tag{6}$$

The functional form for the nonstrange baryonic resonance formation cross sections is assumed to be

$$\sigma(\sqrt{s})=\frac{a(\sqrt{s}/\sqrt{s_{th}}-1)^b d}{(\sqrt{s}/c-1)^2+d^2}. \tag{7}$$

All parameters except the one-Δ production cross section are listed in Tables I and II for each isospin channel where all cross sections are given in mb and $\sqrt{s_{th}}$ denotes a threshold. The one-Δ production cross section $\sigma_1(NN\rightarrow N\Delta(1232))$ is parametrized with the following functional form:

TABLE II. Resonance cross section parameters for $I=0$, π_s denotes *s*-wave pion production.

Channel	a	b	c	d	$\sqrt{s_{th}}$
$\sigma_0(NN\rightarrow NN^*)$	166.60600	2.10128	2.34635	0.284955	2.162
$\sigma_0(NN\rightarrow\Delta(1232)\Delta(1232))$	39.99770	1.83576	2.40348	0.288931	2.252
$\sigma_0(NN\rightarrow\Delta(1232)\Delta^*)$	56.32490	2.00679	2.71312	0.362132	2.528
$\sigma_0(NN\rightarrow N^*N^*)$	2.14575	0.21662	3.40108	0.252889	2.438
$\sigma_0(NN\rightarrow\Delta^*\Delta^*)$	4.14197	1.67026	3.75133	0.476595	2.804
$\sigma_0(NN\rightarrow NN\pi_s)$	78.868103	0.746742	1.25223	0.404072	2.014

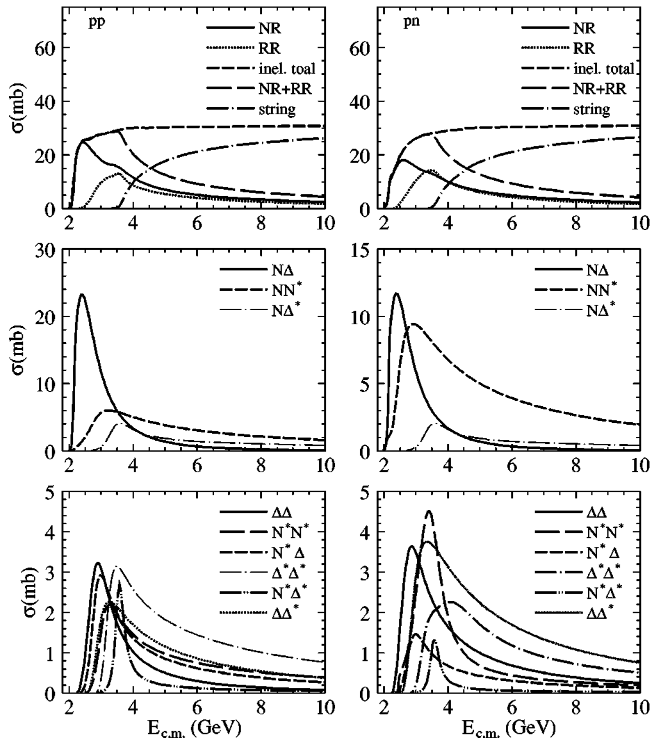

FIG. 2. The resonance production cross sections for pp (left panels) and pn (right panels) reactions as functions of c.m. energies. In the upper panels, the total one-resonance (NR), double-resonance (RR), total resonance (NR+RR), total inelastic cross section, and string formation cross sections are shown. In the middle and the lower panels, each one-resonance production branch and double-resonance production branch is plotted.

$$\sigma_1(NN\rightarrow N\Delta(1232)) = \frac{0.0052840\sqrt{\sqrt{s}/2.0139999-1}}{(\sqrt{s}-2.11477)^2+0.0171405^2} + \frac{28.0401(\sqrt{s}/2.124-1)^{0.480085}}{((\sqrt{s}/2.06672)-1)^2+0.576422^2}, \tag{8}$$

in order to ensure correct threshold behavior. The pionic fusion cross section ($pp\rightarrow d\pi^+$) has been fitted as

$$\sigma(pp\rightarrow d\pi^+) = \frac{0.14648(\sqrt{s}/2.024-1)^{0.20807}}{((\sqrt{s}/2.13072)-1)^2+0.042475^2} + \frac{0.12892(\sqrt{s}/2.054-1)^{0.08448}}{((\sqrt{s}/2.18138)-1)^2+0.059207^2}. \tag{9}$$

In actual simulations, we have effectively included the cross section of the $NN\rightarrow \pi d$ into the Δ production cross section for simplicity. Similarly the s-wave pion production channels $NN\rightarrow NN\pi_s$ are simulated as the $N(1440)$ production.

In Fig. 2 we show the contributions of nonstrange baryonic resonance cross sections for different partial channels as functions of c.m. energies. The upper panels of Fig. 2 show the one-resonance production cross section $NN\rightarrow NR$ (solid lines), two-resonance production cross section $NN\rightarrow RR$ (dotted lines), and the sum of NR and RR cross sections (long-dashed lines) for pp (left panels) and pn (right panels) reactions. Total inelastic cross sections are filled up by the resonance productions up to about $E_{\mathrm{c.m.}}=4$ GeV, while at CERN SPS energies, string excitation is dominated. The dot-dashed lines in the upper panels of Fig. 2 express the string excitation cross sections for pp and pn. At AGS energies corresponding to the invariant mass $\sqrt{s}\sim 5$ GeV, the contributions of the resonance productions and string productions are approximately the same in the first nucleon-nucleon collision in our parametrization. The collision spectrum in BB collisions, however, is spread in broad energy range for Au+Au collision as shown in Ref. [16], due to the high baryon density achieved at AGS energies. Low energy cross sections, therefore, are also important in order to treat the dynamics correctly at AGS energies from first chance NN collisions to the final hadronic gas stage.

The cross section for the resonance productions may be written by

$$\frac{d\sigma_{12\rightarrow 34}}{d\Omega} = \frac{(2S_3+1)(2S_4+1)}{64\pi^2 s p_{12}} \times \int\int p_{34}|\mathcal{M}|^2 A(m_3^2)A(m_4^2)d(m_3^2)d(m_4^2), \tag{10}$$

where $S_i, i=3,4$ express the spin of the particles in the final state. The mass distribution function $A(m_i^2)$ for nucleons is just a δ function, while that for resonances is given by the relativistic Breit-Wigner function

$$A(m^2) = \frac{1}{\mathcal{N}}\frac{m_R\Gamma(m)}{(m^2-m_R^2)^2+m_R^2\Gamma(m)^2}. \tag{11}$$

where $\mathcal{N}$ denotes the normalization constant. In this article, we use simply take $\mathcal{N}=\pi$, which is a value in the case of a constant width. The full width $\Gamma(m)$ is a sum of the partial decay width $\Gamma_R(MB)$ for resonance R into mesons M and baryons B which depends on the momentum of the decaying particle [12,16]:

$$\Gamma_R(MB) = \Gamma_R^0(MB)\frac{m_R}{m}\left(\frac{p_{\mathrm{c.m.s.}}(m)}{p_{\mathrm{c.m.s.}}(m_R)}\right)^{2l+1} \times \frac{1.2}{1+0.2\left(\frac{p_{\mathrm{c.m.s.}}(m)}{p_{\mathrm{c.m.s.}}(m_R)}\right)^{2l+1}}, \tag{12}$$

where l and $p_{\mathrm{c.m.s.}}(m)$ are the relative angular momentum and the relative momentum in the exit channel in their rest frame.

The Monte Carlo procedure is as follows. First, final resonance types $\Delta(1232)$, N^* , or Δ^* are chosen using parametrized cross sections and then we determine each resonance

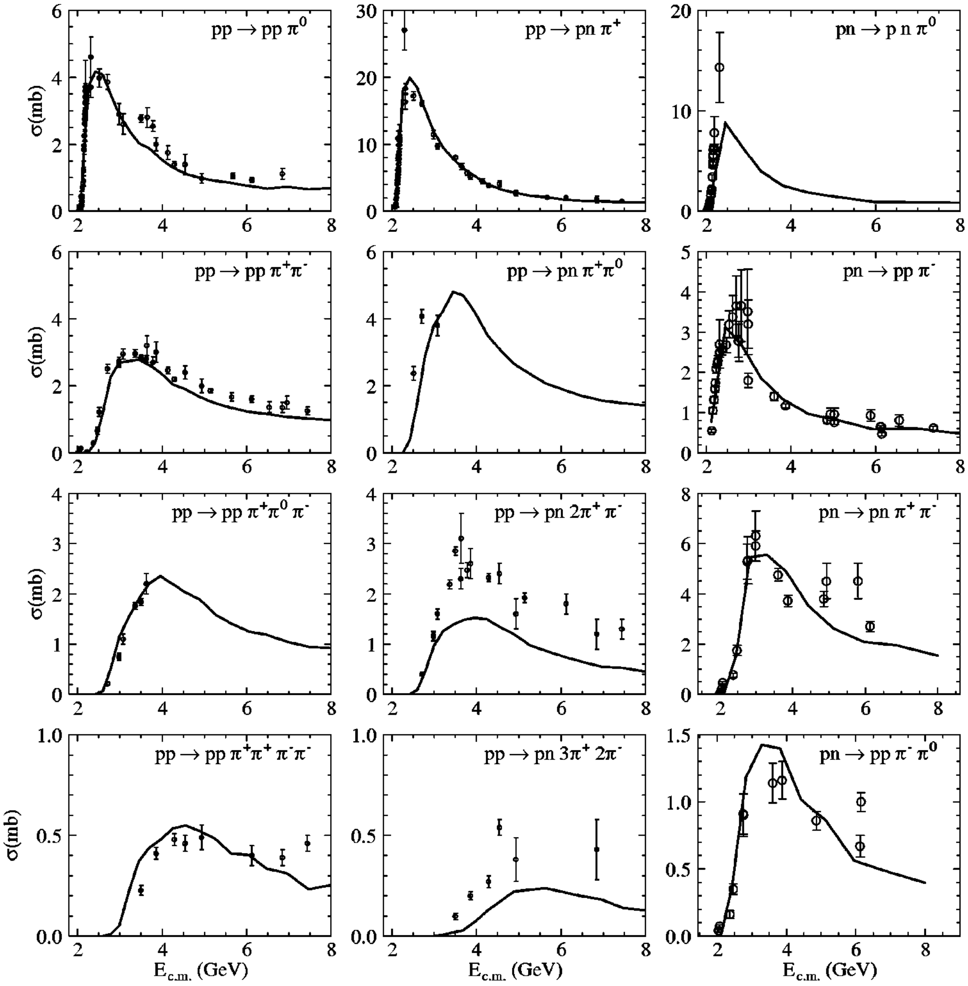

FIG. 3. The energy dependence of the exclusive pion production cross sections for proton-proton and proton-neutron interactions as a function of c.m. energy. Solid lines are the results obtained from the code. Data from Ref. [22].

production channel according to Eq. (10). To do this, we need to know the matrix element $|\mathcal{M}|^2$ for all resonances. In the present model, we make the simple assumption that each resonance production cross section can be selected according to the probability

$$P(R_i,R_j)\sim(2S_i+1)(2S_j+1)\times\int\int p_{ij}A_i(m_i^2)A_j(m_j^2)d(m_i^2)d(m_j^2). \tag{13}$$

Namely, the partial cross section for each resonance state is only governed by the final spins and mass integrals ignoring the resonance state dependence of the matrix element. Once the type of resonances is chosen, we generate the resonance masses according to the distribution, neglecting the mass dependence of the matrix elements in Eq. (10),

$$P(m_3,m_4)dm_3dm_4\sim 4m_3m_4p_{34}A(m_3^2)A(m_4^2)dm_3dm_4, \tag{14}$$

in the reaction $1+2\rightarrow 3+4$, where the mass distribution function $A(m_i)$ should be replaced by the δ function in the case of stable particles in the final state.

In the case of the collisions involving resonance states in the incoming channel, we use the approximation that the inelastic cross sections for resonance production as well as the elastic cross section are the same as the nucleon-nucleon cross sections at the same momentum in the c.m. frame, except for deexcitation processes, $NR\rightarrow NN$ and $RR\rightarrow NN$, whose cross sections are estimated by using the detailed balance described in the next Sec. II C.

Figure 3 shows the energy dependence of the exclusive pion production cross sections in pp (up to five pion production) and pn (up to two pion production) reactions. We compare the results obtained from our simulation with the data in [22]. Overall agreement is achieved in these exclusive pion productions within a factor of two with the above simplification of the common matrix element in Eq. (13). Smooth transition from the resonance picture to the string picture at $E_{\text{c.m.}}=3-4$ GeV is achieved since no irregularity of the energy dependence is present in the calculated results. String excitation law will be described in Sec. II E. In order to get a more satisfactory fit, for example, we can improve the model by introducing different values for the matrix elements for different resonance channels. For example, in Ref. [23], the matrix elements are fitted to reproduce the pion production cross sections up to two-pion productions as well as the η production cross section assuming that they are independent of masses but dependent on species.

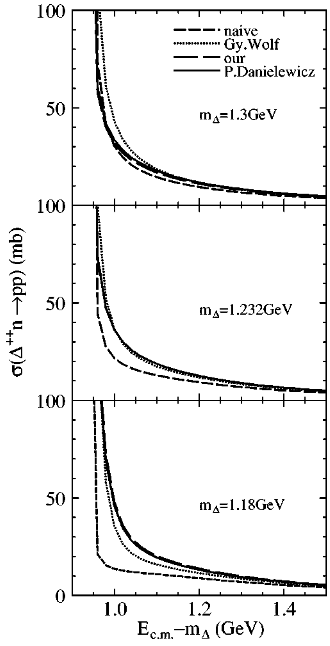

FIG. 4. The cross section for $\Delta^{++}n\to pp$ calculated using the different descriptions for the detailed balance as a function of $\sqrt{s}-M_\Delta$, where M_Δ is the mass of ingoing Δ. The short-dashed lines correspond to the results of the formula which does not take the Δ width into account. The results of the cross sections obtained using the formula in Refs. [26] and [24] are shown by dotted and full lines, respectively. The long-dashed lines correspond to the results using Eq. (18).

C. Detailed balance

In the process of resonance absorption, we use a generalized detailed balance formula [24–26] which takes the finite width of the resonance mass into account. The time-reversal invariance of the matrix element leads to the principle of detailed balance. If scattering particles are all stable, the formula is given by

$$\frac{d\sigma_{34\to12}}{d\Omega}=\frac{(2S_1+1)(2S_2+1)}{(2S_3+1)(2S_4+1)}\frac{p_{12}^2}{p_{34}^2}\frac{d\sigma_{12\to34}}{d\Omega}, \tag{15}$$

where S_i denotes the spin of particle i and p_{ij} corresponds to the c.m. momentum of the particles i and j.

The differential cross section for the reaction $(1,2)\to(3,4)$ for the stable particles may be written

$$\frac{d\sigma_{12\to34}}{d\Omega}=\frac{|\mathcal{M}_{12\to34}|^2}{64\pi^2 s}\frac{1}{(2S_1+1)(2S_2+1)}\times\frac{1}{p_{12}}\int\int p_{34}\delta(p_3^2-m_3^2)d(m_3^2)\times\delta(p_4^2-m_4^2)d(m_4^2), \tag{16}$$

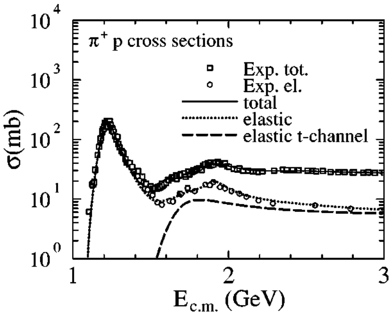

FIG. 5. Parametrization of the total and elastic π^+p cross sections. The data has been taken from [28]. Total and elastic cross sections are assumed to be the sum of s-channel and t-channel resonance and/or string formation processes.

where $|\mathcal{M}_{12\to34}|^2$ represents the spin-averaged matrix element. If the particles have a finite width, we should replace the above δ functions with the certain normalized mass distribution functions $A(m^2)$. Using $|\mathcal{M}_{12\to34}|=|\mathcal{M}_{34\to12}|$, we obtain

$$\frac{d\sigma_{34\to12}}{d\Omega}=\frac{(2S_1+1)(2S_2+1)}{(2S_3+1)(2S_4+1)}\frac{p_{12}^2}{p_{34}}\frac{d\sigma_{12\to34}}{d\Omega}\times\frac{1}{\int\int p_{34}A(m_3^2)A(m_4^2)d(m_3^2)d(m_4^2)}, \tag{17}$$

where we use the relativistic Breit-Wigner function (11) for the mass distribution function $A(m^2)$. The extra factor compared to the usual detailed balance formula increases the absorption cross section. It has been proved that this formula plays an essential role in understanding the $\pi N\Delta$ dynamics [24–26].

In the case of the one-$\Delta(1232)$ absorption cross section, we can write the following formula:

$$\sigma_{N\Delta\to NN'}=\frac{1}{2}\frac{1}{1+\delta_{NN'}}\frac{p_N^2}{p_\Delta}\sigma_{NN'\to N\Delta}\times\left(\int_{(m_N+m_\pi)^2}^{(\sqrt{s}-m_N)^2}p_{\Delta(1232)}A(m^2)dm^2\right)^{-1}. \tag{18}$$

p_N and p_Δ are the final nucleon-nucleon c.m. momentum and the initial c.m. momentum, respectively. The factor $1/(1+\delta_{NN'})$ in Eq. (18) arises from the identical nature of the final states, and 1/2 comes from spins.

There are some versions of the extended detailed balance formula that are slightly different from each other. For example, Danielewicz and Bertch [24] use the formula

$$\frac{d\sigma_{34\to12}}{d\Omega}=\frac{(2S_1+1)(2S_2+1)}{(2S_3+1)(2S_4+1)}\frac{p_{12}^2}{p_{34}}\frac{m_3}{m_3^R}\frac{m_4}{m_4^R}\frac{d\sigma_{12\to34}}{d\Omega}\times\frac{1}{\int\int p_{34}A(m_3'^2)A(m_4'^2)dm_3'^2dm_4'^2}, \tag{19}$$

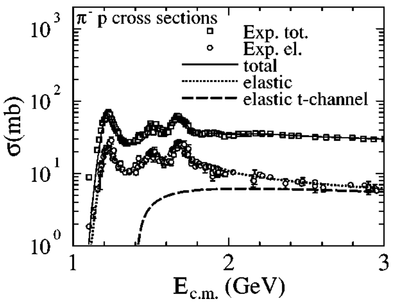

FIG. 6. Parametrization of the total and elastic $\pi^- p$ cross sections. The data has been taken from [28].

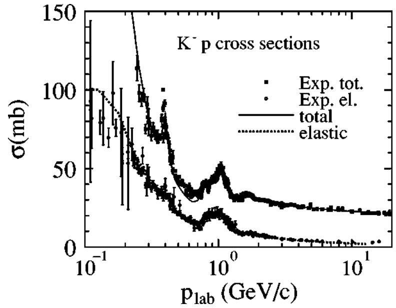

FIG. 7. Parametrization of the total and elastic $K^- p$ cross sections. The data has been taken from [28]. The sum of the *s*-channel resonance productions and *t*-channel elastic, *t*-channel charge exchange, and *t*-channel hyperon production cross sections can describe the data properly at low energies.

where m_i^R denotes the pole mass of the resonance *i*, while Wolf, Cassing, and Mosel [26] use

$$\frac{d\sigma_{34\to 12}}{d\Omega}=\frac{(2S_1+1)(2S_2+1)}{(2S_3+1)(2S_4+1)}\frac{p_{12}^2}{p_{34}^2}\frac{d\sigma_{12\to 34}}{d\Omega}\times\frac{1}{\int\int A(m_3^2)A(m_4^2)dm_3^2dm_4^2}. \tag{20}$$

We have checked that these formulas give similar results to ours. Figure 4 shows the comparisons between the different formulas of the cross sections for the reaction $\Delta^{++}n\to pp$.

D. Meson-baryon, meson-meson collisions

We now turn to the explanation of meson-baryon (MB) and meson-meson (MM) collisions. We also use the resonance/string excitation model for MB and MM collisions.

The total cross section for the πN incoming channel is assumed to be decomposed to

$$\sigma_{tot}(s)^{\pi N}=\sigma_{BW}(s)+\sigma_{el}(s)+\sigma_{s\text{-}S}+\sigma_{t\text{-}S}(s), \tag{21}$$

where $\sigma_{el}(s)$, $\sigma_{BW}(s)$, $\sigma_{s\text{-}S}(s)$, and $\sigma_{t\text{-}S}(s)$ denote the *t*-channel elastic cross section, the *s*-channel resonance formation cross section with the Breit-Wigner form, and the *s*-channel and *t*-channel string formation cross sections, respectively. We neglect the *t*-channel resonance formation cross section at an energy range of $\sqrt{s}\lesssim 2$ GeV. The *t*-channel elastic cross section $\sigma_{el}(s)$ was determined so that the sum of the elastic component of the *s*-channel Breit-Wigner cross section $\sigma_{BW}(s)$ and *t*-channel elastic cross section $\sigma_{el}(s)$ reproduces the experimental elastic data for πN interaction. Above the $\Delta(1232)$ region, the *t*-channel elastic cross section becomes nonzero in our parametrization (Figs. 5 and 6). String formation cross sections $[\sigma_{s\text{-}S}(s)$ and $\sigma_{t\text{-}S}(s)]$ are determined to fill up the difference between the experimental total cross section and $\sigma_{BW}(s)+\sigma_{el}(s)$. We calculate the resonance formation cross section $\sigma_{BW}(s)$ using the Breit-Wigner formula [27,11] (neglecting the interference between resonances),

$$\sigma(MB\to R)=\frac{\pi(\hbar c)^2}{p_{\text{c.m.}}^2}\sum_R |C(MB,R)|^2\times\frac{(2S_R+1)}{(2S_M+1)(2S_B+1)}\times\frac{\Gamma_R(MB)\Gamma_R(\text{tot})}{(\sqrt{s}-m_R)^2+\Gamma_R(\text{tot})^2/4}. \tag{22}$$

The momentum dependent decay width (12) is also used for the calculation of the decay width in Eq. (22). S_R, S_B, and S_M denote the spin of the resonance, the decaying baryon, and meson, respectively. The sum runs over resonances, $R=N(1440)\sim N(1990)$ and $\Delta(1232)\sim\Delta(1950)$. Actual values for these parameters are taken from the Particle Data Group [28] and are adjusted within an experimental error bar to get a reasonable fit for MB cross sections. The results of the fit are shown in Figs. 5 and 6. It has been shown that inclusion of resonances plays an important role in studying strangeness production in AGS and SPS energies [11] and (K^-,K^+) reactions [29]. In fact, strangeness production cross sections for resonance-*N* incoming channels are found to be much larger than that for the πN channel. This would be effective to explain the strangeness enhancement observed in heavy ion collisions within a rescattering scenario.

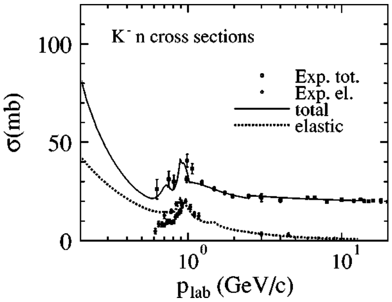

FIG. 8. Parametrization of the total and elastic $K^- n$ cross sections. Parametrizations of the low energy part of the cross section where data are absent are addressed by Ref. [45]. The data have been taken from [28].

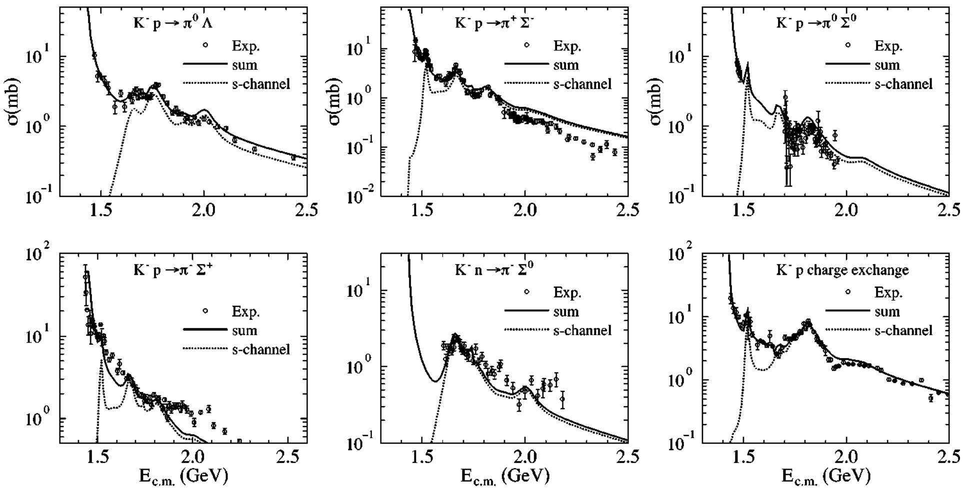

FIG. 9. The energy dependence of the exclusive hyperon production cross sections $K^-p \to \pi^0\Lambda$, $K^-p \to \pi^-\Sigma^+$, $K^-p \to \pi^+\Sigma^-$, $K^-n \to \pi^-\Sigma^0$, $K^-n \to \pi^0\Sigma^0$, and charge exchange cross section $K^-p \to K^0 n$ used in the model are shown by the full lines together with *s*-channel (dotted) contributions. Circles are data from Ref. [46].

Since the $\bar{K}N$ interaction has some exoergic channels such as $\bar{K}N \to \pi Y$, we need to include additional terms:

$$\sigma_{tot}(s)^{\bar{K}N} = \sigma_{BW}(s)+\sigma_{el}(s)+\sigma_{\mathrm{ch}}(s) + \sigma_{\pi Y}(s)+\sigma_{s\text{-}S}(s)+\sigma_{t\text{-}S}(s), \tag{23}$$

where $\sigma_{\mathrm{ch}}(s)$ and $\sigma_{\pi Y}(s)$ denote *t*-channel charge exchange reaction and *t*-channel hyperon production cross sections which are also fixed by the requirement that the sum of *t*-channel contributions and Breit-Wigner contributions reproduce experimental data. The Breit-Wigner formula enables us to calculate experimentally unmeasured cross sections such as $\rho N \to \Lambda K$. For the calculation of $\sigma_{BW}(s)$, we include hyperon resonances, $R=\Lambda(1405) \sim \Lambda(2110)$ and $\Sigma(1385) \sim \Sigma(2030)$. The total and elastic cross sections for $\bar{K}N$ interactions used in JAM are plotted in Figs. 7 and 8 in comparison with experimental data [28].

The symbol $\sigma_{\pi Y}(s)$ in Eq. (23) is the sum of *t*-channel pion hyperon production cross sections $\bar{K}N \to \pi Y$, $Y = \Lambda, \Sigma$. In Fig. 9, we plot the cross sections of hyperon productions and charge exchange cross sections as well as Breit-Wigner contributions fitted in our model. The cross section for the inverse processes such as $\pi Y \to \bar{K}N$ is calculated using the detailed balance formula.

The *KN* incoming channel cannot form any *s*-channel resonance due to its quark contents. Therefore the total cross section can be written within our model as follows:

$$\sigma_{tot}(s)^{KN} = \sigma_{t\text{-}R}(s)+\sigma_{el}(s)+\sigma_{\mathrm{ch}}(s)+\sigma_{t\text{-}S}(s), \tag{24}$$

where $\sigma_{t\text{-}R}(s)$ is *t*-channel resonance formation cross section. Total, elastic, and charge exchange cross sections used in our model are shown in Fig. 10. In the present version of JAM, only $KN \to K\Delta$, $KN \to K(892)N$, and $KN \to K(892)\Delta$ are explicitly fitted to experimental data [22] and fitted results are shown in Fig. 11.

In meson-meson scattering, we also apply the same picture as that in meson-baryon collisions:

$$\sigma_{tot}(s)=\sigma_{BW}(s)+\sigma_{t\text{-}R}(s)+\sigma_{el}(s)+\sigma_{s\text{-}S}(s)+\sigma_{t\text{-}S}(s). \tag{25}$$

The difference between the experimental inelastic cross section and resonance cross sections at energies above resonance region for the meson-baryon and meson-meson collisions is attributed to the string formation cross section where $1/\sqrt{s}$ energy dependence of $\sigma_{s\text{-}S}(s)$ is used [12].

For the cross sections for which no experimental data are available, we calculate the total and elastic cross sections by using the additive quark model [11,16,30]

$$\sigma_{\mathrm{tot}} = \sigma_{NN}\left(\frac{n_1}{3}\right)\left(\frac{n_2}{3}\right)\left(1-0.4\frac{n_{s1}}{n_1}\right)\left(1-0.4\frac{n_{s2}}{n_2}\right), \tag{26}$$

$$\sigma_{el} = \sigma_{\mathrm{tot}}^{2/3}(\sigma_{el}^{NN}/\sigma_{NN}^{2/3}), \tag{27}$$

where σ_{NN}, σ_{el}^{NN} express nucleon-nucleon total and elastic cross sections, and n_i, n_{si} are the number of quarks and *s* quarks contained in the hadron, respectively. This expression works well above the resonance region where the cross section becomes flat.

For the *t*-channel resonance production cross sections $\sigma_{t\text{-}R}(s)$, we do not fit experimental data explicitly in this work except for the *NN* reaction and one and two pion production in the *KN* reaction, because of the vast body of the possibilities for the final states. Instead, we simply determine

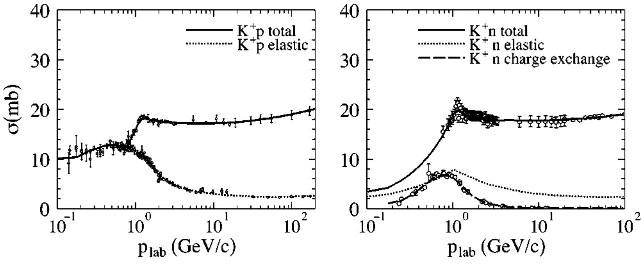

FIG. 10. Parametrization of the total and elastic K^+p and K^+n cross sections as well as the charge exchange cross section in K^+n interaction. The data have been taken from [28].

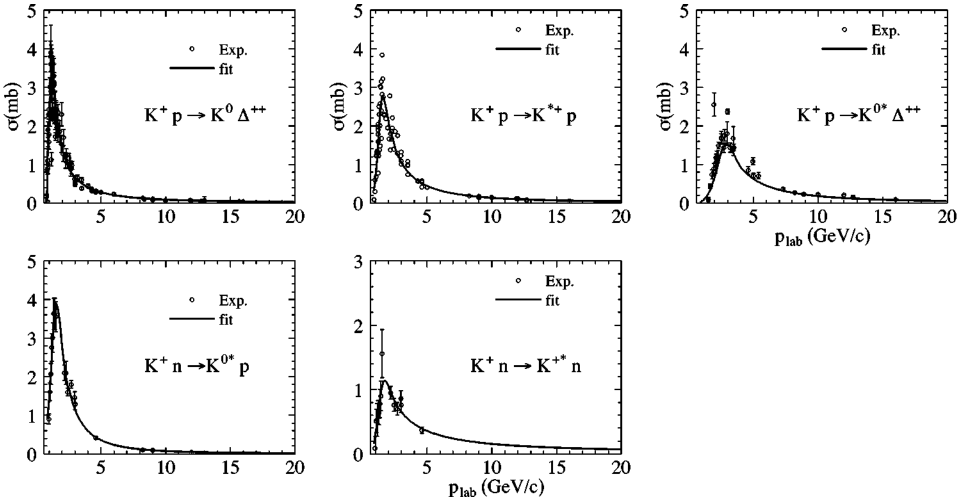

FIG. 11. Parametrization of the Δ, K^* productions cross sections in K^+p and K^+n interactions. The data are from Ref. [22].

the outgoing resonance types according to the spins S_3, S_4 in the final state and phase space for the production of resonances R_3 and R_4

$$P(R_3,R_4) \propto (2S_3+1)(2S_4+1)p_{34}(s)^2, \tag{28}$$

where $p_{34}(s)$ denotes the c.m. momentum in the final state. If the incoming channel involves resonances, their ground state particles are also considered in the final state. Once the outgoing resonance types are determined, we generate masses according to the Breit-Wigner distribution.

For the angular dependence in the processes of *t*-channel resonance production $\sigma_{t\text{-}R}(s)$, we use

$$\frac{d\sigma_{t\text{-}R}(s)}{dt} \sim \exp(bt), \tag{29}$$

and the slope parameter b for the energy range of $\sqrt{s} > 2.17$ GeV is parametrized by

$$b = 2.5 + 0.7\ln(s/2), \tag{30}$$

with invariant mass squared s given in units of GeV^2. We use the same parametrization presented in Ref. [31] for the energy below $\sqrt{s} < 2.17$ GeV for the *t*-channel resonance productions. The elastic angular distribution is also taken from Ref. [31] for $\sqrt{s} < 10$ GeV and from PYTHIA [20] for $\sqrt{s} > 10$ GeV.

E. String formation and fragmentation

At an energy range above $\sqrt{s} > 4-5$ GeV, the (isolated) resonance picture breaks down because the width of the resonance becomes wider and the discrete levels get closer. The hadronic interactions at the energy range $4\text{–}5 < \sqrt{s} < 10\text{–}100$ GeV where it is characterized by the small transverse momentum transfer is called ''soft process,'' and string phenomenological models are known to describe the data for such soft interactions well. The hadron-hadron collision leads to a stringlike excitation longitudinally. In actual description of the soft processes, we follow the prescription adopted in the HIJING model [4], as described below.

In the center-of-mass frame of two colliding hadrons, we introduce light-cone momenta defined by

$$p^+ = E + p_z, \quad p^- = E - p_z. \tag{31}$$

Assuming that beam hadron 1 moves in the positive *z* direction and target hadron 2 moves negative *z* direction, the initial momenta of both the hadrons are

$$p_1 = (p_1^+, p_1^-, 0_T), \quad p_2 = (p_2^+, p_2^-, 0_T). \tag{32}$$

After exchanging the momentum $(q^+, q^-, \boldsymbol{p}_T)$, the momenta will change to

$$p_1' = ((1-x^+)P^+, x^-P^-, \boldsymbol{p}_T),$$

$$p_2' = (x^+P^+, (1-x^-)P^-, -\boldsymbol{p}_T), \tag{33}$$

where $P^+ = p_1^+ + p_2^+ = P^- = p_1^- + p_2^- = \sqrt{s}$ (in the c.m. frame). The string masses will be

$$M_1^2 = x^-(1-x^+)s - p_T^2, \quad M_2^2 = x^+(1-x^-)s - p_T^2, \tag{34}$$

respectively. Minimum momentum fractions are $x_{min}^+ = p_2^+/P^+$ and $x_{min}^- = p_1^-/P^-$. For light-cone momentum

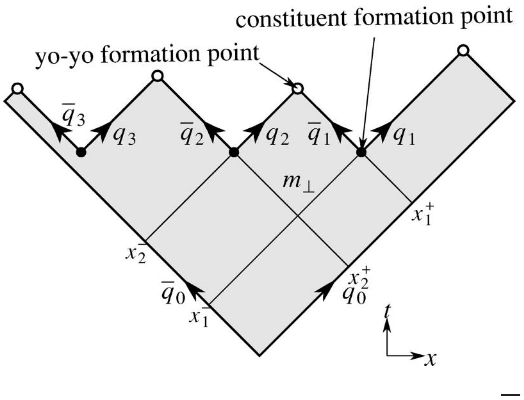

FIG. 12. Space-time picture of the motion in a simple $q\bar{q}$ system and an illustration of how two breakups of the string result in the production of a hadron.

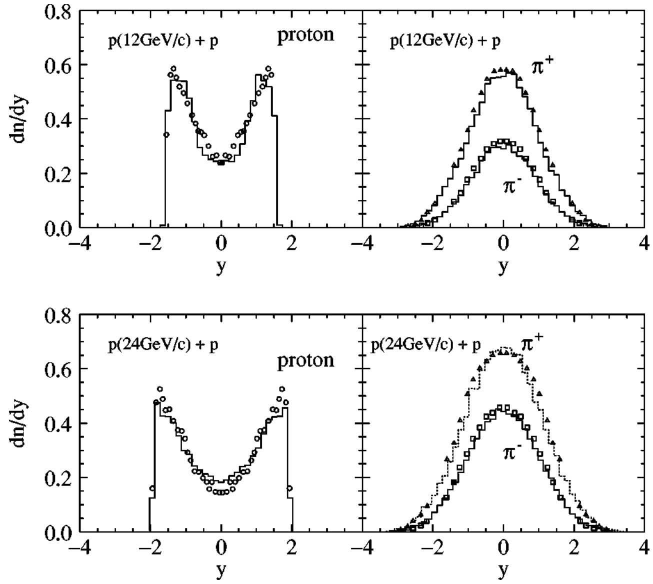

FIG. 13. The rapidity distributions for protons (circles), π^+ (triangles), and π^- (squares) in pp collisions at 12 GeV/c (upper panel) and 24 GeV/c (lower panel). Histograms are the results obtained from our calculation. The data are from Ref. [35].

transfer for the nondiffractive events, we use the same distribution as that in DPM [5] and HIJING [4]:

$$P(x^{\pm})=\frac{(1.0-x^{\pm})^{1.5}}{(x^{\pm 2}+c^2/s)^{1/4}} \tag{35}$$

for baryons and

$$P(x^{\pm})=\frac{1}{(x^{\pm 2}+c^2/s)^{1/4}((1-x^{\pm})^2+c^2/s)^{1/4}} \tag{36}$$

for mesons, where $c=0.1$ GeV is a cutoff. For single-diffractive events, in order to reproduce experimentally observed mass distribution dM^2/M^2, we use the distribution

$$P(x^{\pm})=\frac{1}{(x^{\pm 2}+c^2/s)^{1/2}}. \tag{37}$$

The same functional form as the HIJING model [4] for the soft $\boldsymbol{p}_T$ transfer at low $p_T<p_0$ is used:

$$f(\boldsymbol{p}_T)=\{(p_T^2+c_1^2)(p_T^2+p_0^2)(1+e^{(p_T-p_0)/c_2})\}^{-1}, \tag{38}$$

where $c_1=0.1$ GeV/c, $p_0=1.4$ GeV/c, and $c_2=0.4$ GeV/c, to reproduce the high momentum tail of the particles at energies $E_{lab}=10$–20 GeV.

The strings are assumed to hadronize via quark-antiquark or diquark-antidiquark creation using the Lund fragmentation model PYTHIA6.1 [20]. Hadron formation points from a string fragmentation are assumed to be given by the yo-yo formation point [32] which is defined by the first meeting point of created quarks. The yo-yo formation time is about 1 fm/c assuming the string tension $\kappa=1$ GeV/fm at AGS energies.

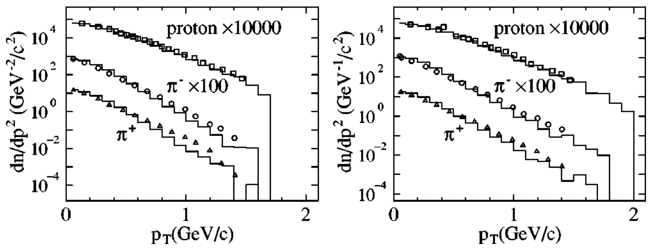

FIG. 14. The transverse momentum distributions for protons (squares), π^+ (triangles), and π^- (circles) in pp collisions at 12 GeV/c (left panel) and 24 GeV/c (right panel). Histograms are the results obtained from our calculation. The data are from Ref. [35].

In the Lund string model, space-time coordinates and energy-momentum coordinates for the quarks are directly related via the string tension [33,34]. Let us consider one-dimensional massless $q\overline{q}$ string in the c.m. frame as illustrated in Fig. 12. If $x_i^{\pm}=t_i\pm x_{zi}$ denotes the light-cone coordinates of the ith production point, then the light cone momenta $p_i^{\pm}=E_n\pm p_{zi}$ of the ith rank hadron, which is produced by the energy-momentum fraction z_i from $(i-1)$th string $p_i^+=z_i p_{i-1}^+$, are fixed by

$$p_i^+=\kappa(x_{i-1}^+-x_i^+),\quad p_i^-=\kappa(x_i^- - x_{i-1}^-), \tag{39}$$

with initial value

$$x_0^+=\frac{W}{\kappa},\quad x_0^-=0, \tag{40}$$

where W corresponds to the string initial invariant mass. Using the relation $p_i^+p_i^-=m_{i\perp}^2$ with $m_{i\perp}$ being the transverse mass of the ith hadron, we have the recursion formulas [33]

$$x_i^+=(1-z_i)x_{i-1}^+,\quad x_i^-=x_{i-1}^-+\left(\frac{m_{i\perp}}{\kappa}\right)^2\frac{1-z_i}{z_i}\frac{1}{x_i^+}. \tag{41}$$

Therefore, yo-yo formation points are obtained as

$$x_i^{yo\text{-}yo}=(x_{i-1}^+,x_i^-), \tag{42}$$

and constituent formation points,

$$x_i^{const}=(x_i^+,x_i^-). \tag{43}$$

In RQMD [12], the formation points of hadrons are calculated as the average of the two $q\overline{q}$ production point as

$$x_i^{RQMD}=\left(\frac{x_i^+ + x_{i-1}^+}{2},\frac{x_i^- + x_{i-1}^-}{2}\right). \tag{44}$$

In UrQMD [16], the yo-yo formation point (42) is used. Clearly, one can see that

$$x_i^{const}<x_i^{RQMD}<x_i^{yo\text{-}yo}. \tag{45}$$

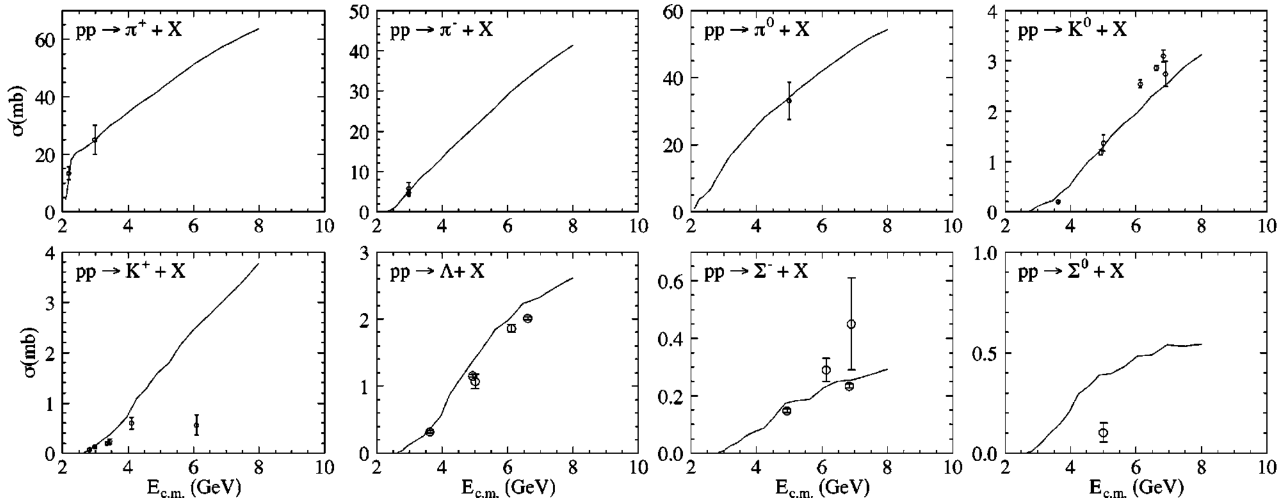

FIG. 15. The energy dependence of the inclusive production cross sections for pions, hyperons, and kaons for the proton-proton interaction as a function of c.m. energy. Solid lines are the results obtained from our model. The data are from Ref. [22].

However, we have checked that at AGS energies, a difference in the definitions of hadron formation points (42),(43),(44) does not affect the final results at all.

In Fig. 13, the calculated rapidity distributions of protons, positive, and negative pions for proton-proton collisions at 12 GeV/c and 24 GeV/c are shown with the data from Ref. [35]. The proton stopping behavior and the pion yields are well described by the present model. Within our model, fast protons come from resonance decays and midrapidity protons from string fragmentation of the Lund model (PYTHIA6.1 [20]) with the default parameter which determines the probability of diquark breaking at these energies. Anisotropic angular distribution in a resonance decay is taken into account assuming Gaussian p_T distribution [12] with a mean value of 0.35 GeV/c^2.

As reported in HIJING [4], an extra low p_T transfer to the constituent quarks is important to account for the high p_T tails of the pion and proton distributions at energies $p_{\mathrm{lab}} \sim 20$ GeV/c^2. As shown in Fig. 14, the present model also reproduces the proton and pion transverse momentum distributions reasonably well at $p_{\mathrm{lab}} = 12$ GeV/c^2 and 24 GeV/c^2.

In addition, the present model also describes well the energy dependence of the particle production cross sections, as shown in Fig. 15. Here we show the incident energy dependence of the inclusive data for π^+, π^-, π^0, K^0, K^+, Λ, Σ^-, and Σ^0 production from proton-proton interactions in comparison with the experimental data [22].

The comparisons shown until now in Figs. 2–13 show that the combination of particle production mechanisms by the resonance decay and the string decay enables us to explore a wide incident energy region from a few hundred MeV to a few ten GeV, with reasonably well-fitted inclusive as well as exclusive cross sections, which are essential inputs in cascade models.

F. Simulation procedure

The basic equation that we have to solve in the hadronic cascade model is the relativistic Boltzmann type equation. In this section, we explain our treatment of time development of the reaction and actual Monte Carlo procedure in the code for completeness, because the details may be different in several computer codes.

In the current verion of JAM, we include only two body collisions, $2 \to 2$, $2 \to 1$ and decay $1 \to n$, where $n = 2,3,\ldots$, in the collision term of the Boltzmann equation.

(i) The initial state is constructed as follows. The nucleons in the nucleus are distributed according to the appropriate Fermi distribution. Then Fermi motion of nucleons is assigned according to the local Fermi momentum $p_f = \hbar(3/2\pi^2\rho(\boldsymbol{r}))^{1/3}$. The initialized phase-space is then boosted.

(ii) The nucleons are propagated along classical trajectories until they interact (two-body scattering, absorption, or decay). The interaction probabilities are determined by the method of so-called ‘‘closest distance approach;’’ if the minimum relative distance b_{rel} for any pair of particles becomes less than the interaction range specified by

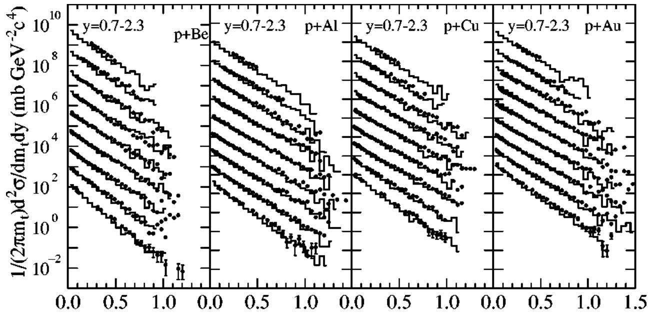

FIG. 16. Invariant cross sections of protons from $p+\mathrm{Be}$, $p+\mathrm{Al}$, $p+\mathrm{Cu}$, and $p+\mathrm{Au}$ collisions at 14.6 GeV/c. The calculated results from the cascade model (histogram) are compared with the E802 data from Ref. [41]. For proton induced collisions (upper panel), the rapidity interval is $y=0.7$ (bottom spectrum) to $y=2.3$ (top spectrum) with $\delta y = 0.2$. The spectra are increased by a factor of 10 from bottom to upper.

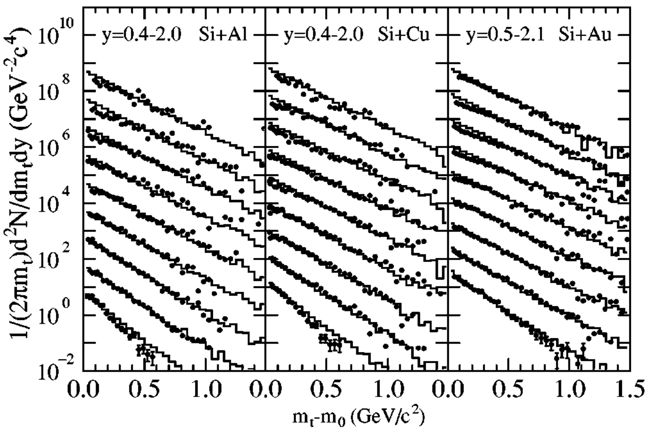

FIG. 17. Invariant cross sections of protons from central Si+Al ($b \leqslant 1.79$ fm), Si+Cu ($b \leqslant 2.2$ fm), and Si+Au ($b \leqslant 2.9$ fm), collisions at 14.6 GeV/c. The calculated results from the cascade model (histogram) are compared with the E802 data from Ref. [42]. For Si+Al and Si+Cu collisions, the rapidity interval is $y = 0.4$ to $y = 2.0$ with $\delta y = 0.2$. For Si+Au collisions, the rapidity interval is $y = 0.4$ to $y = 2.0$ with $\delta y = 0.2$. The spectra are increased by a factor of 10 from bottom to upper.

$\sqrt{\sigma(\sqrt{s})/\pi}$, where $\sigma(\sqrt{s})$ is the total cross section for the pair at the c.m. energy $\sqrt{s}$, then particles are assumed to collide. This cascade method has been widely used to simulate high energy nucleus-nucleus collisions [2,8,9,11,14,15,17,16]. However, a geometrical interpretation of the cross section violates causality, and the time ordering of the collisions in general differs from one frame to another. Those problems have been studied by several authors [9,36]. Here we adopt a similar procedure as Refs. [9,37] for the collision criterion to mimic the reference-frame dependence.

The minimum relative distance b_{rel} is defined by the distance in their common c.m. frame. Let us denote the coordinates and momenta of two particles by $x_1 = (t_1, \boldsymbol{x}_1)$, $x_2 = (t_2, \boldsymbol{x}_2)$, and $p_1 = (E_1, \boldsymbol{p}_1), p_2 = (E_2, \boldsymbol{p}_2)$ respectively, where $t_i (i = 1,2)$ denote the production time (the time of the last collision) whose initial values are set to 0. In the c.m. frame of two particles, we have the equation of motion for particles $i = 1,2$

$$\boldsymbol{x}^*_i(t^*) = \boldsymbol{x}^*_i(t^*) + \boldsymbol{v}^*_i(t^* - t^*_i), \tag{46}$$

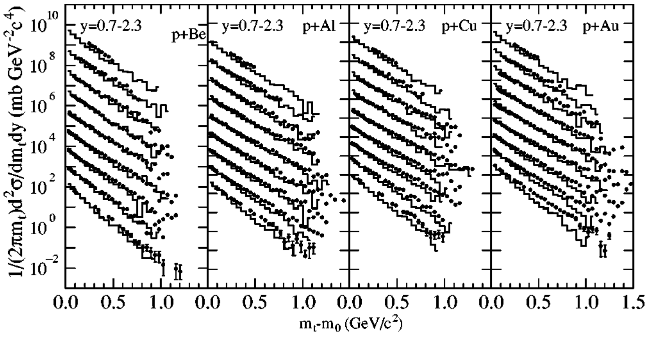

FIG. 18. The Glauber-type calculations compared to the data [41]. The meaning of the figure is the same as Fig. 16.

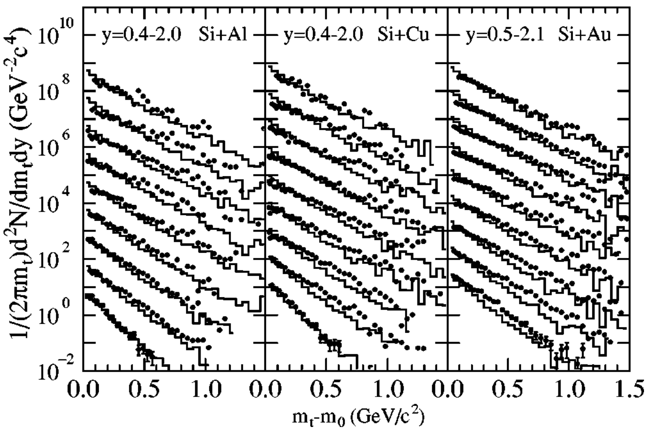

FIG. 19. The Glauber-type calculations compared to the data [42]. The meaning of the figure is the same as Fig. 17.

where asterisks represent quantities in the two-body c.m. frame, and $\boldsymbol{v}^*_i = \boldsymbol{p}^*_i / E^*_i$ are velocities in c.m. frame. Thus the relative distance squared is expressed as a function of c.m. time

$$d^*(t^*) = (\boldsymbol{x}^*_{12} + \boldsymbol{v}^*_{12} t^*)^2, \tag{47}$$

with

$$\boldsymbol{x}^*_{12} = \boldsymbol{x}^*_1 - \boldsymbol{x}^*_2 - \boldsymbol{v}^*_1 t^*_1 + \boldsymbol{v}^*_2 t^*_2, \tag{48}$$

$$\boldsymbol{v}^*_{12} = \boldsymbol{v}^*_1 - \boldsymbol{v}^*_2 . \tag{49}$$

One may calculate the time of minimum relative distance squared b^2_{rel} and the collision time from $d^*(t^*)/dt^* = 0$ as [37]

$$t^*_{min} = -\frac{\boldsymbol{x}^*_{12} \cdot \boldsymbol{v}^*_{12}}{\boldsymbol{v}^{*2}_{12}}, \quad b^2_{rel} = \boldsymbol{x}^{*2}_{12} - \frac{(\boldsymbol{x}^*_{12} \cdot \boldsymbol{v}^*_{12})^2}{\boldsymbol{v}^{*2}_{12}}. \tag{50}$$

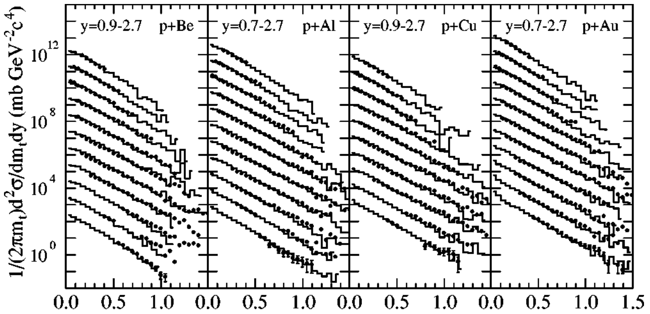

FIG. 20. Invariant cross sections of positive pions from p+Be ($0.9 \leqslant y \leqslant 2.7$), p+Al ($0.7 \leqslant y \leqslant 2.7$), p+Cu ($0.9 \leqslant y \leqslant 2.7$), and p+Au ($0.7 \leqslant y \leqslant 2.7$), collisions at 14.6 GeV/c. The calculated results from the cascade model (histogram) are compared with the E802 data from Ref. [41]. The bin of rapidity is 0.2 for all collision systems. The spectra are increased by a factor of 10 from bottom to upper.

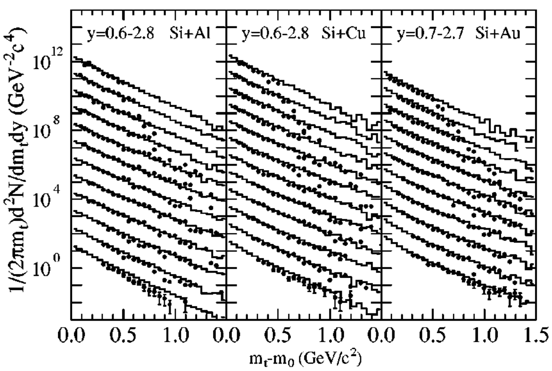

FIG. 21. Invariant cross sections of positive pions from Si+Al $(0.6\leqslant y\leqslant 2.8)$, Si+Cu $(0.6\leqslant y\leqslant 2.8)$, and Si+Au $(0.7\leqslant y \leqslant 2.7)$ collisions at 14.6 GeV/c. The calculated results from the cascade model (histogram) are compared with the E802 data from Ref. [42]. The bin of rapidity is 0.2 for all collision systems. The spectra are increased by a factor of 10 from bottom to upper.

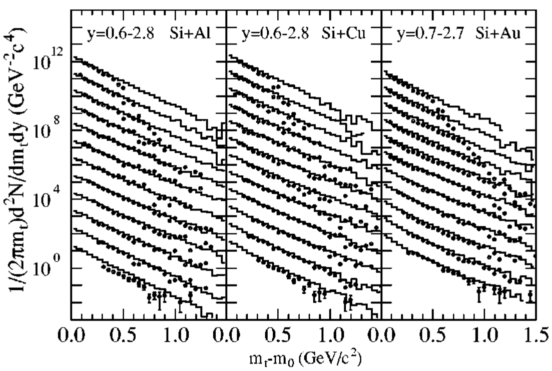

FIG. 23. Invariant cross sections of negative pions from Si+Al $(0.6\leqslant y\leqslant 2.8)$, Si+Cu $(0.6\leqslant y\leqslant 2.8)$, and Si+Au $(0.7\leqslant y \leqslant 2.7)$ collisions at 14.6 GeV/c. The calculated results from the cascade model (histogram) are compared with the E802 data from Ref. [42]. The bin of rapidity is 0.2 for all collision systems. The spectra are increased by a factor of 10 from bottom to upper.

We note that the definition of b_{rel} is also the same as Refs. [16,39,38]. The collision times in the reference frame (computational frame) for each particles are obtained as

$$t_i^{coll}=\gamma(t_{min}^*+\boldsymbol{\beta}\cdot\boldsymbol{r}_i^*),\quad \boldsymbol{r}_i^*=\boldsymbol{x}_i^*+\boldsymbol{v}_i^*(t_{min}^*-t_i^*),\quad (i=1,2), \tag{51}$$

where $\boldsymbol{\beta}=(\boldsymbol{p}_1+\boldsymbol{p}_2)/(E_1+E_2)$ and γ is the corresponding Lorentz γ factor. We assume that the collisions are ordered by the average time $t=1/2(t_1^{coll}+t_2^{coll})$ [9,32]. We have checked that the cascade method described above gives the same results at AGS energies both in the laboratory frame and in nucleus-nuclues c.m. frame calculations.

(iii) Once the collisions are predicted from method (ii), we calculate the partial cross sections explained in the previous section. We generate elastic scattering according to the probability $P_{el}=\sigma_{el}/\sigma_{tot}$. Otherwise, we select whether the collision is soft or hard using the hard cross section calculated by the eikonal formalism for pQCD [4] (note that at AGS energies, the hard cross section is zero). If the soft process is selected, we determine whether this collision is the resonance production or the string formation using our parametrized resonance cross sections. If the resonance production process is selected, we generate resonances and they propagate in space-time. If the string formation process is selected, we generate strings using the DPM type excitation law as explained in Sec. II E and then strings are fragmented using a subroutine of PYTHIA [20] (modified to calculate the positions of hadrons) to obtain the momenta of hadrons as well as the space-time positions of produced hadrons. Newly produced hadrons which have no original constituent quarks begin to propagate at this space-time point. Newly produced hadrons do not interact within the formation time calculated above, but the leading hadrons which have original constituent quarks can scatter further within their formation time with a reduced cross section. For example, the cross section between the leading baryon which has a diquark and formed hadron is $\sigma_{qqh}=2/3\sigma_{hh}$.

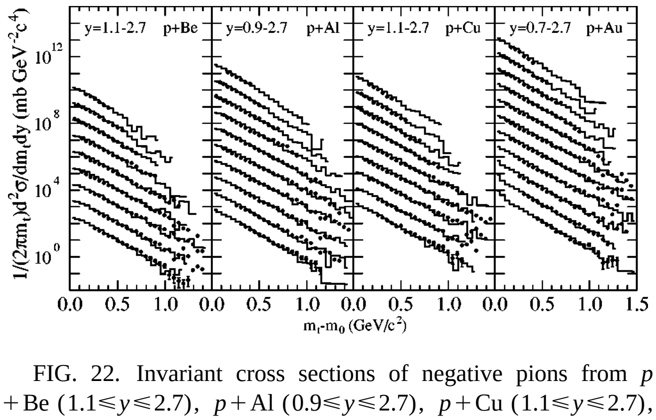

FIG. 22. Invariant cross sections of negative pions from p+Be $(1.1\leqslant y\leqslant 2.7)$, p+Al $(0.9\leqslant y\leqslant 2.7)$, p+Cu $(1.1\leqslant y\leqslant 2.7)$, and p+Au $(0.7\leqslant y\leqslant 2.7)$, collisions at 14.6 GeV/c. The calculated results from the cascade model (histogram) are compared with the E802 data from Ref. [41]. The bin of rapidity is 0.2 for all collision systems. The spectra are increased by a factor of 10 from bottom to upper.

The leading hadron interactions are of importance in order to generate Glauber-like multiple collisions in the initial stage of the reactions in nucleus-nucleus collisions at SPS energies or above. At sufficiently high energies, we might model the nucleus-nucleus collisions as follows. First, to pass through the nucleus together, nucleons scatter according

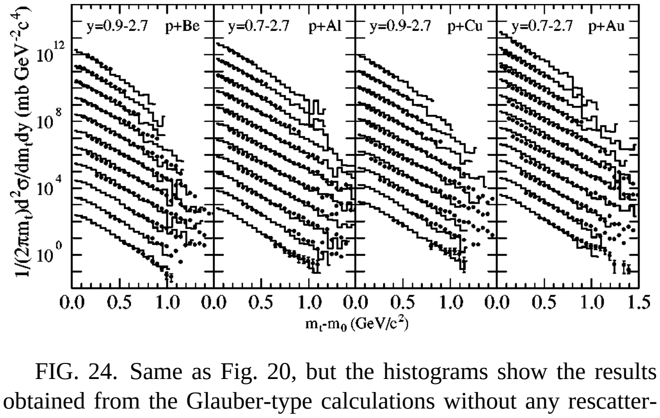

FIG. 24. Same as Fig. 20, but the histograms show the results obtained from the Glauber-type calculations without any rescattering among produced particles.

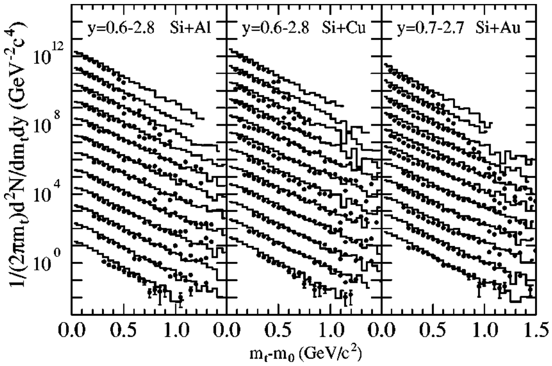

FIG. 25. Same as Fig. 22, but the histograms show the results obtained from the Glauber-type calculations without any rescattering among produced particles.

to the Glauber-type multiple collisions, then final state (secondary) hadron interactions occur before freeze-out. If we can clearly separate this initial multiple collision from the final state hadron interaction, the cascade method described above would approximately give the same collision series for initial multiple scattering. Actually, we have studied the Glauber-type Monte Calro simulation (the same method as HIJING and FRITIOF) and the cascade method without meson-baryon and meson-meson collisions give the same results for the rapidity distributions of protons and produced particles for Pb+Pb central collisions at SPS energy if we use the same elementray inputs. As we will see in Sec. III C, the initial BB collision spectrum which lies around the collision c.m. energy of $4\ \mathrm{GeV} < \sqrt{s} < 6\ \mathrm{GeV}$ is quite similar between Glauber-type calculations and the cascade calculations if final state hadron interactions are negligible (p+Be, p+Al, p+Cu collisions).

III. RESULTS

In the following, we systematically apply our hadronic cascade model (JAM1.0 [40]) to proton, silicon, and gold induced reactions at AGS energies and investigate the effect of cascading by comparing the results obtained by the cascade model with the Glauber-type calculations.

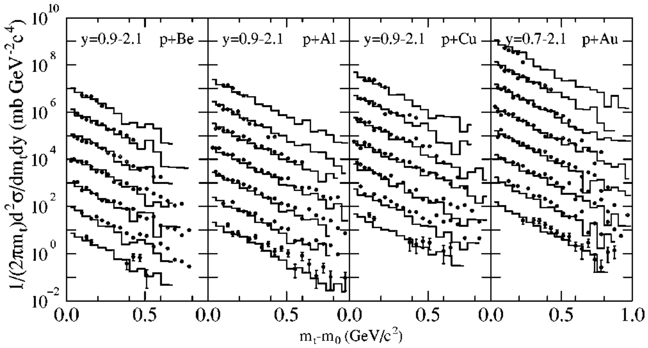

FIG. 26. Comparison of the invariant transverse momentum spectra of K^+ between the cascade model and the experimental data of [41] in p+Be ($0.9 \leqslant y \leqslant 2.1$ with bin size 0.2), p+Al ($0.9 \leqslant y \leqslant 2.1$ with bin size 0.2), p+Cu ($0.9 \leqslant y \leqslant 2.1$ with bin size 0.2), and p+Au ($0.7 \leqslant y \leqslant 2.1$ with bin size 0.2) collisions at 14.6 GeV/c. The spectra are increased by a factor of 10 from bottom to upper.

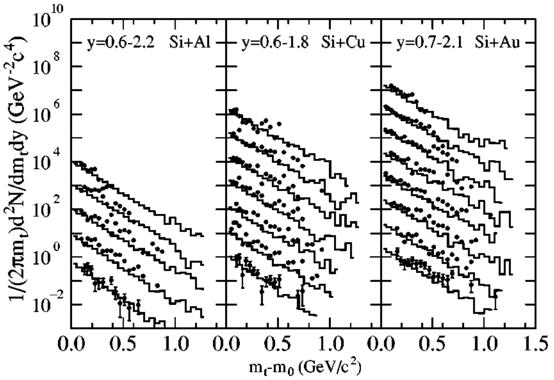

FIG. 27. Comparison of the invariant transverse momentum spectra of K^+ between the cascade model and the experimental data of [42] in Si+Al ($0.6 \leqslant y \leqslant 2.2$ with bin size 0.2), Si+Cu ($0.6 \leqslant y \leqslant 1.8$ with bin size 0.4), and Si+Au ($0.7 \leqslant y \leqslant 2.1$ with bin size 0.2) collisions at 14.6 GeV/c. The spectra are increased by a factor of 10 from bottom to upper.

A. Comparison to E802 data

In this section, we first focus our attention on the proton transverse distributions to check the detailed examination of the collision term and its space-time picture (formation time) used in our model and also to see the transition of the reaction dynamics from proton induced collisions to heavy ion collisions.

We show in Fig. 16 proton invariant transverse mass distributions calculated by our cascade model for the proton induced reactions p+Be, p+Al, p+Cu, p+Au, and in Fig. 17, silicon induced reactions of central Si+Al, Si+Cu, Si+Au at 14.6 GeV/c in comparison to the data from the E802 Collaboration [41,42]. In each figure, spectra are plotted in a rapidity interval of 0.2 and are displayed by multiplying each by a power of 10 from bottom to upper. Si+Al, Si+Cu, and Si+Au data correspond to the central collision with 7% centrality. For the calculations of Si+A (A =Al,Cu,Au) systems, the impact parameter is distributed as

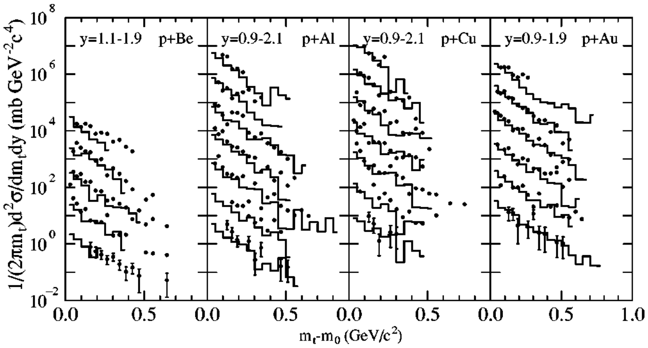

FIG. 28. Comparison of the invariant transverse momentum spectra of K^- in p+Be ($1.1 \leqslant y \leqslant 1.9$ with bin size 0.2), p+Al ($0.9 \leqslant y \leqslant 2.1$ with bin size 0.2), p+Cu ($0.9 \leqslant y \leqslant 2.1$ with bin size 0.2), and p+Au ($0.9 \leqslant y \leqslant 1.9$ with bin size 0.2) collisions at 14.6 GeV/c. The spectra are increased by a factor of 10 from bottom to upper.

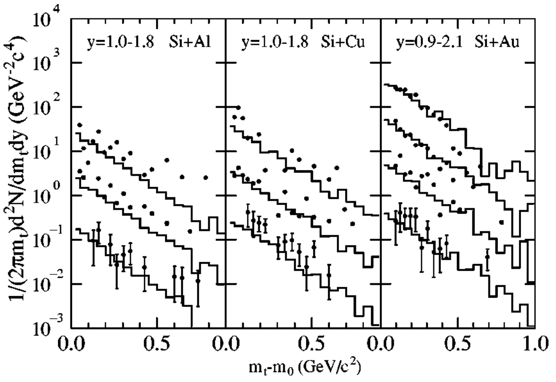

FIG. 29. Comparison of the invariant transverse momentum spectra of K^- in Si+Al ($1.0 \leqslant y \leqslant 1.8$ with bin size 0.4), Si+Cu ($1.0 \leqslant y \leqslant 1.8$ with bin size 0.4), and Si+Au ($0.9 \leqslant y \leqslant 2.1$ with bin size 0.4) collisions at 14.6 GeV/c. The spectra are increased by a factor of 10 from bottom to upper.

follows: $b < 1.797$ fm for Si+Al, $b < 2.2$ fm for Si+Cu, and $b < 2.9$ fm for Si+Au. Our calculations show good agreement with the data in proton induced reactions. In silicon induced reactions, our calculations do a good job of accounting for the experimental data in general. However, we can see some overestimates at low transverse momenta, in particular for the Si+Au system. As a result, our cascade model gives larger proton stopping than the data.

Now we compare the cascade model results with the Glauber-type calculation in order to see the effect of pion rescattering, nucleon cascading, and the consequent deviation from the linear extrapolation of sum of binary nucleon-nucleon collisions to proton-nucleus and nucleus-nucleus collisions. Glauber-type models such as the FRITIOF model [1] have been widely used at higher energies, i.e., more than 200*A* GeV. We use the same method as the FRITIOF model with some modifications. The wounded nucleons become resonances or strings in each nucleon-nucleon collision, and strings can interact again before they fragment. Resonances can be converted to nucleons, and strings are allowed to be deexcited to the minimum string mass. After all binary collisions are completed, strings and resonances are forced to decay. Rescattering of produced particles is not considered. In the present treatment, we have used our parametrization in calculating the probability to excite nucleons to resonances or strings. Figures 18 and 19 show the results obtained by this Glauber-type calculation. In the beam rapidity region, for all systems, good agreement can be seen because the effects of rescattering would be small as expected. For proton-induced reactions, the Glauber-type calculation gives a steeper shape in comparison to the data at midrapidity and target regions. In heavy ion reactions, this deviation is significant at around midrapidity. Rescattering, therefore, is necessary to account for transverse momentum distributions of protons for reactions involving heavy nuclei.

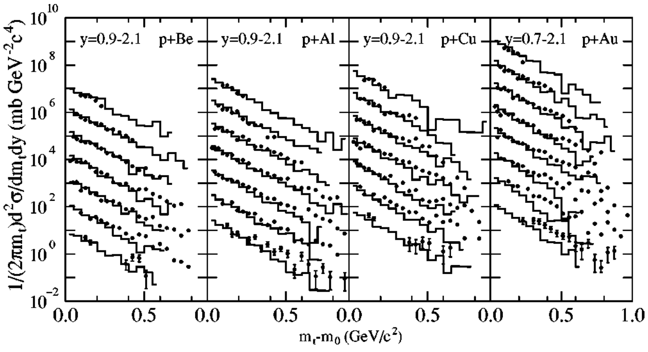

FIG. 30. Glauber-type calculations of invariant cross sections of K^+ for p+Be, p+Al, p+Cu, and p+Au reactions at 14.6 GeV/c in comparison to the E802 data from [41]. The meaning of the figure is the same as Fig. 26.

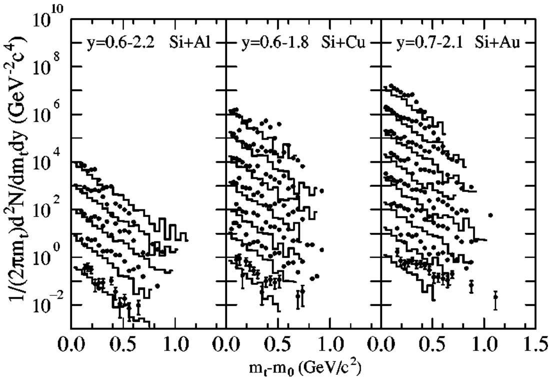

FIG. 31. Glauber-type calculations of the invariant cross sections of K^+ for Si+Al, Si+Cu, and Si+Au reactions at 14.6 GeV/c in comparison to the E802 data from [42]. The meaning of the figure is the same as Fig. 27.

We now turn to the mass dependence of the pion transverse distributions. In Figs. 20–23, we show the calculated π^+ and π^- spectra by histograms together with the E802 data [41,42]. Agreement between the cascade model and the data is very good for the combination of projectile and target, and for both the slope parameter and the absolute value of the cross section.

On the other hand, as shown in Fig. 24 and Fig. 25, Glauber-type calculations reproduce well the data for small mass systems p+Be, p+Al, p+Cu, and Si+Al, and give similar slopes to the experimental data, while the multiplicity of pions in heavy systems is larger than that of the data. This

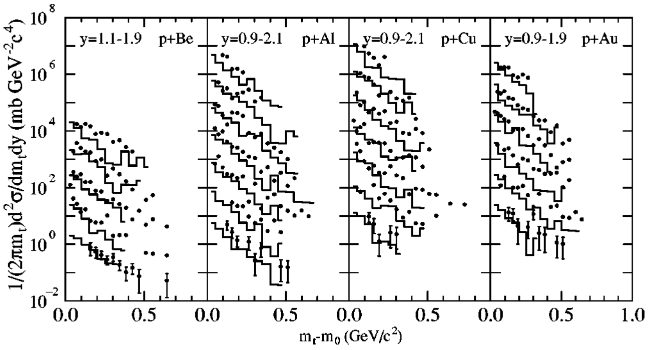

FIG. 32. Glauber-type calculations of invariant cross sections of K^- for p+Be, p+Al, p+Cu, and p+Au reactions at 14.6 GeV/c in comparison to the E802 data from [41]. The meaning of the figure is the same as Fig. 28.

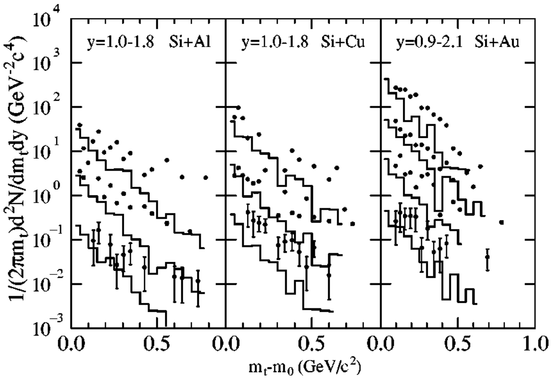

FIG. 33. Glauber-type calculations of invariant cross sections of K^- for $p+$Be, $p+$Al, $p+$Cu, $p+$Au, Si+Al, Si+Cu, and Si+Au reactions at 14.6 GeV/c in comparison to the E802 data from [42]. The meaning of the figure is the same as Fig. 29.

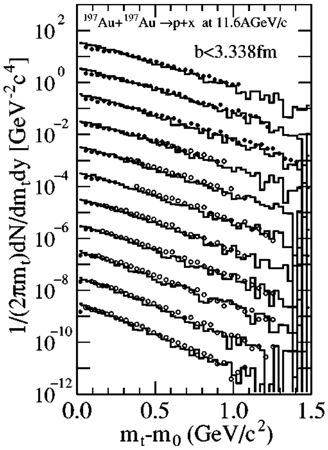

FIG. 34. The result of the cascade model calculation of transverse mass distributions of protons for the central Au+Au collision at 11.6 GeV/c in different rapidity intervals. The spectra are scaled down by a factor of 10 successively from upper corresponding to the c.m. rapidity $y=0.05$ to lower spectrum of $y=1.05$ with the bin width of 0.1. The impact parameter is distributed from 0 to 3.338 fm. The data are from Ref. [43].

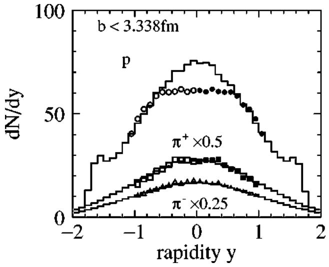

FIG. 35. Comparison of rapidity distributions of protons (circles), positive pions (squares), and negative pions (triangles) between experimental data [43] and the cascade model calculations (histograms) for central Au+Au collision at 11.6 GeV/c. The data for positive pions are scaled down by a factor of 0.5 and for negative pions 0.25. In the cascade calculations, the impact parameter is distributed from 0 to 3.338 fm.

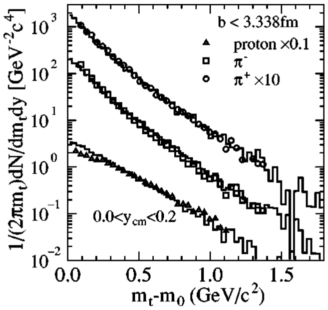

FIG. 36. Transverse mass distributions of protons and pions for the central Au+Au collision at 11.6 GeV/c. The triangles represent the data of protons scaled by a factor of 0.1; squares correspond to π^- data, circles correspond to π^+ data scaled by a factor of 10 from Ref. [43]. Histograms represent the results from the cascade model with impact parameter $b\leqslant 3.338$ fm.

is due to the effect of rescattering in which pions are absorbed during evolution for the large mass systems.

Let us study the kaon and antikaon transverse mass spectra of E802. The calculated transverse mass distributions of K^+ and K^- in the cascade model are compared with the E802 data [41,42] in Figs. 26–29. Figures 30–33 are the results with the Glauber-type calculations for K^+ and K^- invariant transverse momentum distributions. We find more significant differences between the cascade and Glauber results of kaon production than those in proton and pion spectra. This fact shows the importance of the rescattering: As discussed in Sec. II D, some of the exoergic MB reactions, which involve resonances, have very large strangeness production cross sections, and they contribute to K and $\overline{K}$ production, especially in heavy ion reactions [11,29]. Enhancements due to these meson rescatterings are clearly seen in the K^+ and K^- spectra, except for the reactions of $p+$Be and $p+$Al, because there is no meson-baryon collision in Glauber-type calculation.

B. Au+Au collisions

We continue our comparison to E866 experimental data [43] with the truly heavy ion collision Au+Au at 11.6A GeV. Our cascade model calculation with impact parameter $b\leqslant 3.338$ fm is compared to E866 data [43] in Fig.

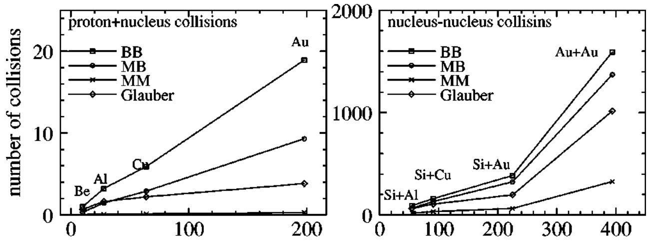

FIG. 37. Mass dependence of the number of BB (open squares), MB (open circles), and MM (open crosses) collisions obtained from the cascade model calculations and Glauber-type calculations (open diamonds) for $p+A$ collisions in the left panel and for Si+A and Au+Au collisions (right panel).

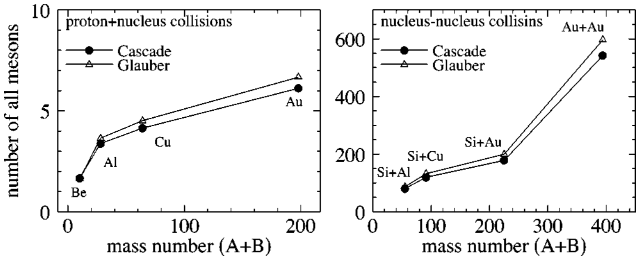

FIG. 38. Mass dependence of the number of total mesons from the cascade model calculations (full circles) and Glauber-type calculations (full triangles) for Si+A (A=Al, Cu, Au), Au+Au collisions (right panel) and for $p+$A (A=Be, Al, Cu, Au) collisions (left panel). Meson multiplicity is reduced by including rescattering.

34 from c.m. rapidity of $y=0.05$ to $y=1.05$ with the rapidity bin of 0.1 scaled down by a factor of 10 from the top to the bottom spectrum. The cascade model results show good agreement with the data at the transverse mass above 0.2 GeV/c^2. The cascade model, however, overpredicts again the proton spectrum in the low transverse momentum region.

In Figs. 35 and 36, we compare the cascade model results with the experimental data by the E802 Collaboration [43] in central Au+Au collisions. Pion multiplicities are in good agreement with data as well as the slopes of both π^+ and π^-. However, the present cascade model does not describe the suppression of protons having low transverse momenta, and consequently it gives stronger stopping of proton than the data. This proton rapidity spectrum for central Au+Au collisions shows an amount of stopping similar to those with other cascade models like RQMD [11], ARC [14], and ART [15]. In addition, the Glauber-type calculation gives the same results for the proton rapidity distribution. Therefore, this defect is not a consequence of the cascade model. Since the deviation of the transverse mass spectrum of heavy hadrons from a single exponential behavior is generally considered as a result of the radial flow, it may be influenced by the nuclear mean field. In fact, it has been found in the works of RQMD [44] and ART [15] nuclear mean field significantly reduces maximum baryon densities of the hadronic matter, and consequently the midrapidity protons become small.

In this work, we have assumed that the elastic and inelastic cross sections involving baryon resonances, except for the deexcitation processes to NN, are the same as that in the NN channel at the same c.m. momentum. However, since the deexcitation cross sections are enhanced due to the generalized detailed balance as explained in Sec. II C, if other cross sections are smaller than those of NN, stopping power may be reduced.

C. Mass dependence of the collision dynamics

In this section, we study the mass dependence of the collision dynamics within the hadronic cascade model. First we present the cascade model results of BB, MB, and MM collision numbers as a function of the system mass $(A+B)$ in comparison to that of Glauber-type calculations.

Figure 37 displays the total collision number of BB (open squares) and MB (open circles) and MM (open crosses) obtained from the cascade calculation together with a Glauber-type calculation (open diamonds) for the $p+$A (left panel) and Si+A (right panel) collisions. When the system becomes bigger, BB collisions are much more frequent in the cascade model than in the Glauber predictions, even in the proton induced collisions. This indicates that there is successive nucleon cascading in the nuclear medium in the cascade model picture. It is interesting to see that the number of BB and MB collisions is almost the same in heavy ion collisions. This seems to be the origin of the pion number suppression, the increase in the proton transverse momentum slope, and the increase in kaon yield.

Indeed we can see the reduction of produced pion multiplicity in the cascade model compared to the Glauber-type calculations as shown in Fig. 38, where the number of total produced mesons is plotted as a function of the system mass

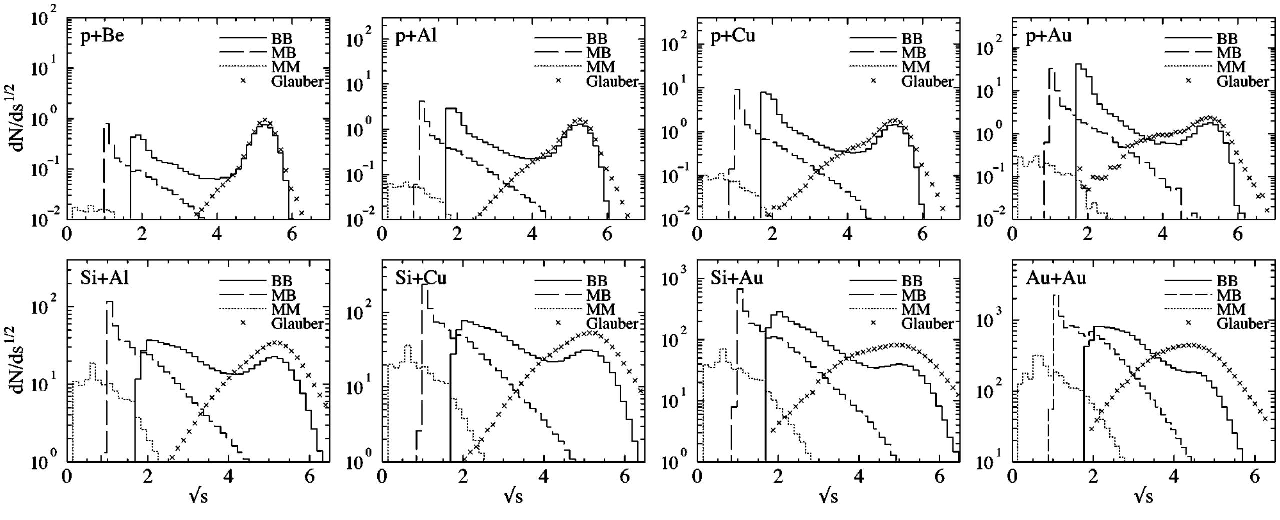

FIG. 39. Collision spectrum of BB (full lines), MB (dashed lines), and MM (dotted lines) collisions from the cascade model calculations and Glauber-type calculations (crosses) for the $p+$Be, $p+$Al, $p+$Cu, $p+$Au, Si+Al, Si+Cu, Si+Au, and Au+Au collisions at AGS energies.

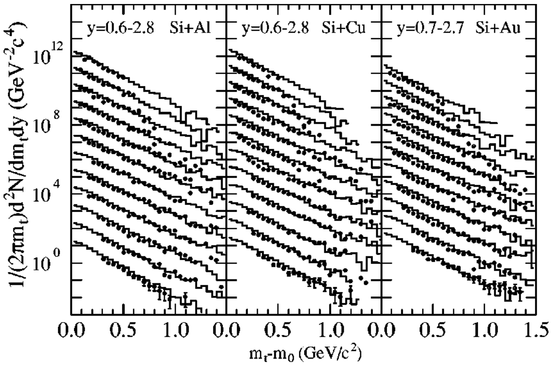

FIG. 40. Same as Fig. 21, but the histograms show the results obtained from the Glauber-type calculations without any rescattering among produced particles.

number. Pions are absorbed mainly in the two-step process in the cascade model. For example, the most important pion absorption path at AGS energies is

$$\pi N \rightarrow \Delta, \quad N\Delta \rightarrow NN. \tag{52}$$

Therefore, a large number of BB and MB collisions are necessary to describe appropriate pion absorptions.

In order to get more detailed information on the mass dependence of the collision dynamics at AGS energies, we display in Fig. 39 the colliding energy spectrum of BB, MB, and MM given by the cascade model together with those from the Glauber-type calculations. The BB collision distributions as a function of invariant mass are very different between the cascade model and the Glauber-type model. The Glauber-type calculations predict the collisions which are spread around the initial NN c.m. energy, while the BB collisions occur at all available collision energies in the cascade model. In both $p+\mathrm{A}$ and $A+B$ reactions, the MB collisions are pronounced in the resonance region ($\sqrt{s} \leqslant 2$ GeV). It is interesting to note that in $p+\mathrm{Au}$ system, the number of low energy BB collisions is much larger than that of $p+\mathrm{Be}$, $p+\mathrm{Al}$, and $p+\mathrm{Cu}$ systems. In $A+B$ systems (bottom of Fig. 39), the collision number grows very quickly; however, the shape of the collision spectrum is similar in all the systems (see Figs. 40, 41).

IV. SUMMARY

We have systematically studied the system mass dependence of the particle distributions at AGS energies with a newly developed cascade model (JAM1.0). The cascade model is shown to provide a good description of the observed data for various combinations of projectile and target without any change of model parameters. The effect of rescattering of produced particles and nucleon cascading is found to be important to explain both the pion yield and the transverse slope, which are demonstrated by comparing the cascade model results with the Glauber-type calculations. Those effects increase the transverse momentum slopes of protons and pions, and reduce the pion yield. The importance of the rescattering among particles is more visible in kaon spectra.

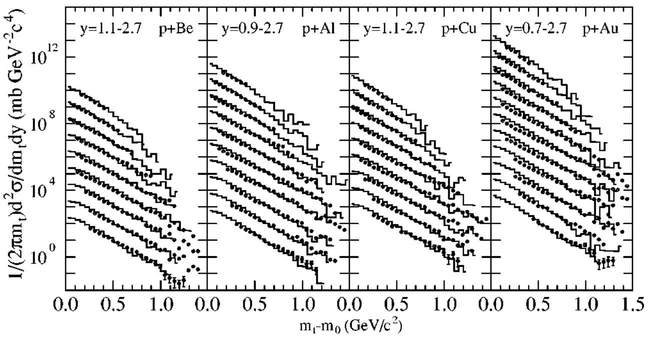

FIG. 41. Same as Fig. 22, but the histograms show the results obtained from the Glauber-type calculations without any rescattering among produced particles.

One of the problems in the hadronic cascade model JAM is that it gives much larger stopping of the protons in nucleus-nucleus collisions. This large stopping is not the consequence of rescattering because the Glauber-type calculation also gives the same amount of baryon stopping. This problem of strong baryon stopping in cascade models has been reported, and proton spectra can be fitted by the inclusion of a nuclear mean field in RQMD [44] and ART [15].

Another possible solution may be to suppress the cross sections such as $\sigma(N_1^* N_2^* \rightarrow N_3^* N_4^*)$, which is assumed to be the same as that in the NN incoming channel at the same c.m. momentum in a present model. These interactions among resonances become important at AGS energies where we have sufficiently dense matter in heavy ion collisions, and the baryon stopping is sensitive to the cross sections in the resonance incoming reactions. In fact, we have checked that if resonance-resonance (BB) cross sections are reduced from the nucleon-nucleon cross section, we get less proton stopping than the present results. Detailed study in this line will be interesting.

ACKNOWLEDGMENTS

One of the authors (Y.N.) would like to thank BNL for the kind hospitality where part of the calculations were done. Y. N. would like to thank Professor H. Stöcker and Dr. H. Sorge for their encouragement, and useful comments. We acknowledge careful reading of the manuscript by Professor R. Longacre.

---

[1] B. Andersson, G. Gustafson, and H. Pi, Z. Phys. C **57**, 485 (1993); H. Pi, Comput. Phys. Commun. **71**, 173 (1992).
[2] Sa Ben-Hao and Tai An, Comput. Phys. Commun. **90**, 121 (1995); Phys. Rev. C **55**, 2010 (1997); Phys. Lett. B **399**, 29 (1997); **409**, 393 (1997).
[3] K. Werner, Z. Phys. C **42**, 85 (1989); Phys. Rep. **232**, 87

(1993).
[4] X. N. Wang and M. Gyulassy, Phys. Rev. D **44**, 3501 (1991); X. N. Wang, Phys. Rep. **280**, 287 (1997); X. N. Wang and M. Gyulassy, Comput. Phys. Commun. **83**, 307 (1994); http://www-nsdth.lbl.gov/∼xnwang/hijing/
[5] A. Capella, U. Sukhatme, C.-I. Tan, and J. Tran Thanh Van, Phys. Rep. **236**, 225 (1994).
[6] A. Shor and R. Longacre, Phys. Lett. B **218**, 100 (1989).
[7] S. Jeon and J. Kapusta, Phys. Rev. C **56**, 468 (1997).
[8] K. Geiger, Phys. Rep. **258**, 238 (1995); Comput. Phys. Commun. **104**, 70 (1997); http://penguin.phy.bnl.gov/∼klaus/
[9] B. Zhang, Comput. Phys. Commun. **109**, 70 (1997); http://nt1.phys.columbia.edu/people/bzhang/ZPC/zpc.html; B. Zhang and Y. Pang, Phys. Rev. C **56**, 2185 (1997); B. Zhang, M. Gyulassy, and Y. Pang, *ibid.* **58**, 1175 (1998).
[10] K. Geiger, Nucl. Phys. **A638**, 551c (1998); D. K. Srivastava and K. Geiger, Phys. Lett. B **422**, 39 (1998); K. Geiger and B. Mueller, Heavy Ion Phys. **7**, 207 (1998); K. Geiger and D. K. Srivastava, Phys. Rev. C **56**, 2718 (1997); K. Geiger and R. Longacre, Heavy Ion Phys. **8**, 41 (1998).
[11] H. Sorge, R. Mattiello, A. Jahns, H. Stöcker, and W. Greiner, Phys. Lett. B **271**, 37 (1991); H. Sorge, L. Winckelmann, H. Stöcker, and W. Greiner, Z. Phys. C **59**, 85 (1993).
[12] H. Sorge, Phys. Rev. C **52**, 3291 (1995).
[13] L. Bravina, L. P. Csernai, P. Levai, and D. Strottman, Phys. Rev. C **50**, 2161 (1994).
[14] Y. Pang, T. J. Schlagel, and S. H. Kahana, Nucl. Phys. **A544**, 435c (1992); Phys. Rev. Lett. **68**, 2743 (1992); S. H. Kahana, D. H. Kahana, Y. Pang, and T. J. Schlagel, Annu. Rev. Nucl. Part. Sci. **46**, 31 (1996).
[15] B. A. Li and C. M. Ko, Phys. Rev. C **52**, 2037 (1995); Phys. Lett. B **382**, 337 (1996); Nucl. Phys. **A630**, 556 (1998); Phys. Rev. C **58**, R1382 (1998); B. A. Li, C. M. Ko, and G. Q. Li, *ibid.* **54**, 844 (1996).
[16] L. A. Winckelmann, S. A. Bass, M. Bleicher, M. Brandstetter, A. Dumitru, C. Ernst, L. Gerland, J. Konopka, S. Soff, C. Spieles, H. Weber, C. Hartnack, J. Aichelin, N. Amelin, H. Stöcker, and W. Greiner, Nucl. Phys. **A610**, 116c (1996); S. A. Bass, M. Belkacem, M. Bleicher, M. Brandstetter, L. Bravina, C. Ernst, L. Gerland, M. Hofmann, S. Hofmann, J. Konopka, G. Mao, L. Neise, S. Soff, C. Spieles, H. Weber, L. A. Winckelmann, H. Stöcker, W. Greiner, C. Hartnack, J. Aichelin, and N. Amelin, Prog. Part. Nucl. Phys. **41**, 225 (1998).
[17] W. Ehehalt and W. Cassing, Nucl. Phys. **A602**, 449 (1996); J. Geiss, W. Cassing, and C. Greiner, nucl-th/9805012.
[18] Y. Nara, N. Otuka, A. Ohnishi, and T. Maruyama, Suppl. Prog. Theor. Phys. **129**, 33 (1997).
[19] H. Weber, C. Ernst, M. Bleicher, L. Bravina, H. Stöcker, and W. Greiner, nucl-th/9808021.
[20] T. Sjöstrand, Comput. Phys. Commun. **82**, 74 (1994); PYTHIA 5.7 and JETSET 7.4 Physics and Manual. http://thep.lu.se/tf2/staff/torbjorn/Welcome.html
[21] Y. Nara, Nucl. Phys. **A638**, 555c (1998).
[22] *Total Cross-Sections for Reactions of High Energy Particles*, edited by A. Baldni, V. Flaminio, W. G. Moorhead, and D. R. O. Morrison (Springer-Verlag, Berlin, 1988), Vols. 12a, 12b.
[23] S. Teis, W. Cassing, M. Effenberger, A. Hombach, U. Mosel, and Gy. Wolf, Z. Phys. A **356**, 421 (1997); M. Effenberger, A. Hombach, S. Teis, and U. Mosel, Nucl. Phys. **A613**, 353 (1997).
[24] P. Danielewicz and G. F. Bertch, Nucl. Phys. **A533**, 712 (1991).
[25] Bao-An Li, Nucl. Phys. **A552**, 605 (1993).
[26] Gy. Wolf, W. Cassing, and U. Mosel, Nucl. Phys. **A552**, 549 (1993).
[27] G. E. Brown, C. M. Ko, Z. G. Wu, and L. H. Xia, Phys. Rev. C **43**, 1881 (1991).
[28] Particle Data Group, R. M. Barnett *et al.*, Phys. Rev. D **54**, 1 (1996).
[29] Y. Nara, A. Ohnishi, T. Harada, and A. Engel, Nucl. Phys. **A614**, 433 (1997).
[30] K. Goulianos, Phys. Rep. **101**, 169 (1983).
[31] K. Niita, S. Chiba, T. Maruyama, T. Maruyama, H. Takada, T. Fukahori, Y. Nakahara, and A. Iwamoto, Phys. Rev. C **52**, 2620 (1995).
[32] A. Bialas and M. Gyulassy, Nucl. Phys. **B291**, 793 (1987).
[33] B. Andersson, G. Gustafson, G. Ingelman, and T. Sjöstrand, Phys. Rep. **97**, 31 (1983).
[34] T. Sjöstrand, Nucl. Phys. **B248**, 469 (1984).
[35] V. Blobel *et al.*, Bonn-Hamburg-München Collaboration, Nucl. Phys. **B69**, 454 (1974).
[36] G. Kortemeyer, W. Bauer, K. Haglin, J. Murray, and S. Pratt, Phys. Rev. C **52**, 2714 (1995).
[37] B. Andersson, A. Tai, and Ben-Hao Sa, Z. Phys. C **70**, 499 (1996).
[38] Gy. Wolf, G. Batko, W. Cassing, U. Mosel, K. Niita, and M. Schäfer, Nucl. Phys. **A552**, 517 (1990).
[39] T. Kodama, S. B. Duarte, K. C. Chung, R. Donangelo, and R. A. M. S. Nazareth, Phys. Rev. C **29**, 2146 (1984).
[40] JAM1.0, source code and its documentation, to be prepared.
[41] T. Abbott *et al.*, E802 Collaboration, Phys. Rev. D **45**, 3906 (1992); Compilation of relativistic heavy-ion data, http://www.nndc.bnl.gov/∼hi_data/rhid.html
[42] T. Abbott *et al.*, E802 Collaboration, Phys. Rev. C **50**, 1024 (1994); Compilation of relativistic heavy-ion data [1].
[43] L. Ahle *et al.*, E802 Collaboration, Phys. Rev. C **57**, R466 (1998).
[44] H. Sorge, R. Mattiello, H. Stöcker, and W. Greiner, Phys. Rev. Lett. **68**, 286 (1992); R. Mattiello, H. Sorge, H. Stöcker, and W. Greiner, Phys. Rev. C **55**, 1443 (1997).
[45] A. S. Rosenthal and F. Tabakin, Phys. Rev. C **22**, 711 (1980).
[46] High-Energy Reactions Analysis Group, CERN Report CERN-HERA 83-01 and 83-02, 1983 (unpublished).